

# Flame–turbulence interactions during flame acceleration using solid and fluid obstacles

Cite as: Phys. Fluids **34**, 106106 (2022); <https://doi.org/10.1063/5.0118091>

Submitted: 03 August 2022 • Accepted: 11 September 2022 • Accepted Manuscript Online: 13 September 2022 • Published Online: 13 October 2022

 Wandong Zhao (赵万东),  Jianhan Liang (梁剑寒),  Ralf Deiterding, et al.



View Online



Export Citation



CrossMark

## ARTICLES YOU MAY BE INTERESTED IN

[Effect of transverse jet position on flame propagation regime](#)

Physics of Fluids **33**, 091704 (2021); <https://doi.org/10.1063/5.0063363>

[Ignition and deflagration-to-detonation transition modes in ethylene/air mixtures behind a reflected shock](#)

Physics of Fluids **34**, 086105 (2022); <https://doi.org/10.1063/5.0103013>

[Effects of fluctuations in concentration on detonation propagation](#)

Physics of Fluids **34**, 076101 (2022); <https://doi.org/10.1063/5.0096965>



Physics of Plasmas   Physics of Fluids  
Special Topic: Turbulence in Plasmas and Fluids  
Submit Today!

# Flame–turbulence interactions during flame acceleration using solid and fluid obstacles

Cite as: Phys. Fluids **34**, 106106 (2022); doi: [10.1063/5.0118091](https://doi.org/10.1063/5.0118091)

Submitted: 3 August 2022 · Accepted: 11 September 2022 ·

Published Online: 13 October 2022



View Online



Export Citation



CrossMark

Wandong Zhao (赵万东),<sup>1,2</sup> Jianhan Liang (梁剑寒),<sup>1,a)</sup> Ralf Deiterding,<sup>2</sup> Xiaodong Cai (蔡晓东),<sup>1,a)</sup> and Xinxin Wang (王鑫鑫)<sup>1</sup>

## AFFILIATIONS

<sup>1</sup>Science and Technology on Scramjet Laboratory, College of Aerospace Science and Engineering, National University of Defense Technology, Changsha 410073, China

<sup>2</sup>Aerodynamics and Flight Mechanics Research Group, University of Southampton, Boldrewood Innovation Campus, Southampton SO16 7QF, United Kingdom

<sup>a)</sup>Authors to whom correspondence should be addressed: [jhleon@vip.sina.com](mailto:jhleon@vip.sina.com) and [cai-chonger@hotmail.com](mailto:cai-chonger@hotmail.com)

## ABSTRACT

A combination of solid and transverse jet obstacles is proposed to trigger flame acceleration and deflagration-to-detonation transition (DDT). A numerical study of this approach is performed by solving the reactive Navier–Stokes equations deploying an adaptive mesh refinement technique. A detailed hydrogen–air reaction mechanism with 12 species and 42 steps is employed. The efficiency and mechanisms of the combined obstacles on the flame acceleration are investigated comprehensively. The effects of multiple jets, jet start time, and jet stagnation pressure on the DDT process are studied. Results show that there is a 22.26% improvement in the DDT run-up time and a 33.36% reduction in the DDT run-up distance for the combined obstacles compared to that having only solid obstacles. The jet acts as an obstruction by producing a suitable blockage ratio and introducing an intense turbulent region due to the Kelvin–Helmholtz instability. This leads to dramatic flame–turbulence interactions, increasing the flame surface area dramatically. The dual jet produces mushroom-like vortices, leading to a significantly stretched flame front and intensive Kelvin–Helmholtz instabilities, and therefore, these features produce a high flame acceleration. As the jet operation time decreases, the jet obstacle almost changes its role from both physical blockage ratio and turbulence and vorticity generator to a physical blockage ratio. There is a moderate jet stagnation pressure that reduces the run-up time to detonation and run-up distance to detonation in the obstacle-laden chamber. While further increasing the jet stagnation pressure, it does not have a positive effect on shortening the detonation transition.

Published under an exclusive license by AIP Publishing. <https://doi.org/10.1063/5.0118091>

## NOMENCLATURE

AMR	Adaptive mesh refinement
AMROC	Adaptive mesh refinement in object-oriented C++
Br	Blockage ratio
CJ	Chapman–Jouguet
DDT	Deflagration-to-detonation transition
jet	Jet obstacle
K–H	Kelvin–Helmholtz
$L_{DDT}$	DDT run-up distance
MUSCL	Monotone upwind scheme for conservation laws
PDE	Pulse detonation engine
Pts	Grid points
R–T	Rayleigh–Taylor
Roe–HLL	Roe–Harten–Lax–van Leer

SW	Shock wave
SWACER	Shock wave amplification by coherent energy release
$T_{DDT}$	DDT run-up time
VN	von Neumann
ZND	Zel’dovich–Neumann–Döring
2D	Two-dimensional
3D	Three-dimensional

## I. INTRODUCTION

Detonation combustion is considered as thermodynamically particularly efficient because of its constant volume combustion behavior, which would result in high thermal cycle efficiency.<sup>1–3</sup> The detonation combustion mode can be utilized in different engineering applications, including the pulse detonation engine (PDE) and rotating detonation

engine, which have a high potential to augment the aerospace thrust performance for the future advanced propulsion systems. Such systems should be capable of operating within a confined combustion duct, resulting in a lower weight and cost.<sup>4</sup> Although detonation combustors have a higher thermodynamic performance than traditional deflagration systems, employing detonation combustion is still a challenge as a result of its unstable behavior.<sup>5–8</sup>

One of the key obstacles to the detonation combustion engine is how to obtain a robust and stable detonation initiation.<sup>6</sup> Tremendous efforts have been made to ignite detonation combustion, such as direct ignition,<sup>9,10</sup> pre-detonator ignition underlying within a small-scale tube,<sup>11–13</sup> and deflagration-to-detonation transition (DDT) approaches.<sup>13–16</sup> Manipulating detonation combustion through a direct ignition will require significant transient deposition of energy for the mixture. Therefore, it is still difficult and impractical to carry out a detonation initiation in a practical environment using the high and transient energy release from an external device. The pre-detonator ignition approach can be easily operated for a typical combustion chamber. However, it still encounters some drawbacks including the requirement for an extra gas mixture supply system, which increases the complexity of the device and the possibility of failure in transition to detonation in the combustor compared to other typical ignition methods.<sup>17,18</sup> Generally, a detonation wave achieved by the DDT process is considered a more reliable and efficient method in combustors because of their lower requirement of ignition energy and easy operation within the chamber.<sup>2,6</sup> There are still some fundamental drawbacks with the DDT approach, including a long start time and large combustor length required for a successful DDT.<sup>19</sup> As such, obtaining a rapid onset of detonation is a major issue that requires further investigation.

Past studies have demonstrated that maintaining a highly turbulent flow within the combustion chamber is crucial to accelerate the flame propagation speed. The traditional method of turbulence generation consists mainly of multiple fixed objects that are placed into the combustion tube, for example, rings, orifice plates, wedges, and Shchelkin spirals.<sup>20–24</sup> Hence, a large number of investigations were carried out to study the effect of physically fixed solid obstacles for turbulence induction and consequently promoting the flame acceleration and DDT process.<sup>14,25–29</sup> These solid obstructions act as a blockage for the flame and fluid flow, resulting in a high flame propagation velocity as well as triggering the Kelvin–Helmholtz (K–H) instabilities shedding from the tips of the obstacles. Such an instability leads to the generation of large turbulent eddies that interact with the flame front, which, in turn, increase the flame surface area and flame acceleration accordingly, owing to the high energy release rate.<sup>30</sup> After these series of flame accelerations, a compression wave is formed as a response to the rate of the specific volume of mixture across the flame. A subsequent shock wave (SW) is generated within the chamber when the compression waves coalesce together, which further preheats the unburned material.<sup>30–32</sup> At the subsequent stage, the fixed obstructions provide shock reflection and shock focusing, which leads to the generation of hot spots around the obstacles.<sup>30</sup> The energy released by the autoignition of these localized hot spots can enhance the DDT process.<sup>30,33</sup> Subsequently, the detonation occurs when a hot spot is generated in the space region between the leading shock and the flame front due to the shock wave, amplified by the coherent energy release (SWACER) mechanism associated with the gradients within the

mixture, such as temperature, density, and pressure.<sup>30,34,35</sup> However, when operating a particular detonation engine such as PDE, these obstacles, which are fixed within the chamber, result in pressure losses and introduce thermal reservoirs.<sup>16,17,36,37</sup> This leads to ~25% engine thrust loss as confirmed by previous research.<sup>2,38</sup>

To overcome the above shortcoming of the obstacle-laden chamber in the DDT process, the fluidic transverse jet approach is introduced, which provides a similar function as the solid obstacle and has lower pressure loss.<sup>17,39</sup> These fluidic crossflow jets have an advantage to be adjusted easily to form different turbulent flows and eddies by changing the jet width and stagnation pressure, which can efficiently control the DDT process.<sup>40</sup> Prior work on the effects of a transverse jet in crossflow on the DDT process was successfully produced by Knox *et al.*<sup>17,41</sup> They demonstrated that the transverse jet acts as a physical obstruction and introduces a high level of turbulence within the chamber. Their result showed that jet compositions of air and mixture do not have a significant influence on the DDT run-up time ( $T_{DDT}$ ) and DDT run-up distance ( $L_{DDT}$ ). The transverse jet composed of kerosene–air, however, has a dramatically positive influence on flame acceleration and detonation initiation.<sup>42</sup> Subsequently, several experimental studies were carried out to evaluate the effect of a single transverse jet on the flame acceleration at an early stage of the DDT process.<sup>43–45</sup> It was found that in comparison with the solid obstacle's case, the transverse jet is more effective in introducing a transition from a laminar flame to a turbulent flame.<sup>43–45</sup> In addition, a transverse jet with a supersonic flow was injected into the combustion chamber, resulting in a successful DDT process with significantly shorter  $T_{DDT}$  and  $L_{DDT}$ .<sup>46</sup> In the recent experiment and numerical research by Peng *et al.*<sup>16</sup> on flame acceleration and DDT, the detonation wave was triggered by a single or two crosswise transverse jets composed of a methane–oxygen mixture in smooth tubes. The result revealed that the transverse jet could reduce the required length of the detonation tube and shorten the start time of DDT occurrence.<sup>16</sup> Moreover, other jet parameters (including the composition, temperature and pressure, as well as the exit width of the jet) influencing the flame acceleration and the DDT process in smooth combustion tubes were comprehensively investigated.<sup>47</sup> Most recently, the non-reactive transverse jets, composed of carbon dioxide, helium, or nitrogen, were also injected into the smooth chamber to investigate the acceleration of a methane–oxygen flame. The obtained results demonstrated that the non-reactive jet promotes a rapid flame acceleration, resulting in a shorter distance of the DDT formation.<sup>48,49</sup>

In the current literature, there is no consideration of the combined effect of fluid and solid obstacles on the flame acceleration and DDT. The combination approach would couple the different advantages from two kinds of obstacles to shorten  $T_{DDT}$  and  $L_{DDT}$ . In addition, only a few studies have evaluated the start time and the required length of detonation initiation by transverse jets. Furthermore, the effect of the start time of the jet stream after ignition on the DDT process has not been studied. Hence, this work aims at closing the above-mentioned gaps through a detailed numerical analysis of combined solid and transverse jet obstructions in a combustion tube. The results obtained for the combined configuration are compared against those obtained for a solid obstacle configuration. Additionally, the effect of the dual jet stream and the start time of the transverse jet on the flame acceleration and DDT processes were further investigated. The current research is an extension of our previous study.<sup>50</sup> The numerical

simulations were performed by solving the reactive Navier–Stokes equations together with a detailed hydrogen–air reactive kinetics model consisting of 12 species and 42 reaction steps. The structured adaptive mesh refinement (AMR) technique was employed in the calculating framework<sup>51</sup> to enable high-resolution simulations.

## II. COMPUTATIONAL MODEL AND NUMERICAL METHODS

### A. Computational configuration

A two-dimensional (2D) computational domain was employed in the current study to investigate the entire flame acceleration and DDT process. The 2D configuration enables us to reduce the computational cost while resolving the prominent features influencing the DDT processes, as demonstrated in previous studies.<sup>30,40</sup> The computational domain (Fig. 1) is a rectangular tube of  $L_x \times L_y = 700 \times 20 \text{ mm}^2$ . Three configurations termed A, B, and C were considered. Configuration A incorporates multiple solid obstructions to accelerate the flame. As presented in Fig. 1, the pipe is confined on the left, upper, and lower sides, while it allows free outflow on the right side of the domain. The upper and lower sides of the tube are arranged with several typical rectangular solid obstacles with a size of  $d \times h$ . The interval between the solid obstacles is  $S$ , and the distance between the left boundary to the first obstacle  $L$  is set to be 48 mm. To prompt the occurrence of DDT, a high spacing of  $S = 50 \text{ mm}$  is considered between the solid obstacles for the formation of Mach stems, as reported in previous studies.<sup>32</sup> With the obstacle's height of  $h = 3 \text{ mm}$ , the blockage ratio ( $Br$ ) is 0.3, which is within the recommended range for flame acceleration.<sup>52</sup> Hence, a slightly lower  $Br$  is considered to balance the flame acceleration ratio and lower the pressure loss, as discussed in the Sec. I. The width of the obstacle is  $d = 2 \text{ mm}$ . Ten pairs of solid plates were employed on the upper and lower side of the computational domain. For configuration B [see Fig. 1(b)], the arrangement for

configuration A was modified such that one of the solid obstructions is replaced by a single crosswise transverse jet located at the bottom wall, and the combined solid and transverse jet obstacles were adopted to stimulate the flame acceleration. The width of the jet is also the same as the solid, in order to control the extra influence on the flame acceleration and DDT. Configuration C [see Fig. 1(c)] incorporates multiple jets to detect the effect of multiple jets on the flame acceleration. Adiabatic and no-slip wall boundary conditions were specified on all walls, including the upper and lower walls as well as solid obstacles. It is noted that the width of the current research is close to the critical limit<sup>6</sup> with respect to the detonation cell size (1–1.6 cm) of the initial mixture, and also, Gamezo *et al.*<sup>14</sup> have revealed that the combustion wave experiences a choking flame regime propagating about half of Chapman–Jouguet (CJ) speed. In our previous study<sup>50</sup> on the same configuration as Fig. 1(b), it is demonstrated that the choking flame regime is formed when there is an early flame turbulent interaction when the jet position is located at  $X = 50 \text{ cm}$ . Moreover, in the current jet position, no choking flame region is observed.

Several cases were considered, as shown in Table II. Cases 1 and 2 were employed to study the influence of the combined fluid/solid obstacles compared to the solid obstacle only. The composition of the transverse jet is a premixed stoichiometric  $\text{H}_2/\text{air}$  with temperature  $T_{\text{jet}} = 298 \text{ K}$ , whereas it has a slightly high stagnation pressure of  $P_{\text{jet}} = 0.35 \text{ MPa}$ . Furthermore, dual impact jet obstacles arranged at  $L_x = 100 \text{ mm}$ , as used in configuration C in Fig. 1, were also utilized to study the effect of multiple jets on the flame acceleration and DDT processes, corresponding to case 3. The start time of the transverse jet was set to  $t = 0.001 \text{ ms}$  in cases 2 and 3. Additionally, cases 4 and 5 were considered to study the effect of jet start time after the ignition of the premixed mixture on the flame acceleration, which was set as  $t = 0.25$  and  $t = 0.5 \text{ ms}$ , respectively, with a motivation to detect the perturbation time of turbulence generation. To detect the stagnation pressure of the transverse jet on the DDT process, cases 6–8 employed lower as well as higher stagnation pressure compared to case 2, corresponding to case 6  $Br_j = 2.0$ , case 7  $Br_j = 5.0$ , and case 8  $Br_j = 6.5$ , where  $Br_j$  represents the  $Br$  generated by the transverse jet, where the relation is assumed as  $Br_j = P_{\text{jet}}/P_0$ . These three cases are aimed at studying the effect of the strength of perturbation caused by the jet on the DDT process. The width of the transverse jet was kept the same as the solid obstruction to control the external influence on the flame acceleration and DDT.

The combustion chamber was filled with a premixed stoichiometric  $\text{H}_2$ –air mixture under standard atmospheric pressure and temperature with  $P = 0.1 \text{ MPa}$  and  $T = 298 \text{ K}$ . A semi-sphere hot spot with a radius of  $r = 4 \text{ mm}$  on the left boundary with  $T = 2500 \text{ K}$  and  $P = 0.1 \text{ MPa}$  is employed to ignite the perfectly stirred mixture. A similar approach has been considered in the previous literature.<sup>14,16,32,53</sup> A low-pressure source prevents a high propagation velocity of the flame front and the formation of the shock wave at the early stage of the flame propagation, enabling us to analyze the effect of the obstacle only. The detailed parameters of the initial premixed mixture are given in Table I. The theoretical parameters of the Chapman–Jouguet (CJ) condition and laminar flame properties for the current mixture in Table I are obtained from Cantera.<sup>54</sup> The detonation cell size is calculated by an empirical correlation model provided by Ng *et al.*<sup>55</sup> that considers the Zel'dovich–Neumann–Döring (ZND) reaction zone as well as the reaction structure.

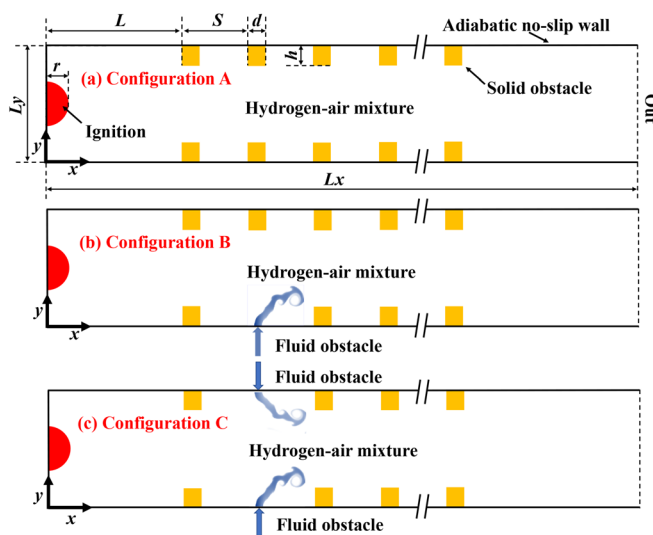


**FIG. 1.** Schematic illustration of the computational domain for the flame acceleration and DDT. (a) Configuration A: only the solid obstacles are adopted; (b) Configuration B: a single jet and solid obstacles are employed for flame acceleration; (c) Configuration C: the dual impact jet and solid obstacles are applied.



**TABLE I.** The thermodynamic properties of hydrogen–air mixture and the corresponding CJ parameters.

Quantity	Value	Definition
$P_0$	0.1 MPa	Initial pressure
$T_0$	298 K	Initial temperature
$M$	21 g/mol	Molecular weight
$P_{VN}$	$27.7P_0$ MPa	Pressure at von Neumann state
$T_{VN}$	$5.14T_0$ K	Temperature at von Neumann state
$\rho_{VN}$	$2.109 \text{ kg/m}^3$	Density at von Neumann state
$S_l$	$\approx 2.98 \text{ m/s}$	Laminar flame speed
$L_l$	$\approx 0.35 \text{ mm}$	Laminar flame thickness
$P_{CJ}$	$15.58P_0$ MPa	CJ pressure
$T_{CJ}$	$9.875T_0$ K	CJ temperature
$\rho_{CJ}$	$1.5205 \text{ kg/m}^3$	CJ density
$V_{CJ}$	$1965 \text{ m/s}$	CJ speed
$X_d$	$1\text{--}1.6 \text{ cm}$	Detonation cell width

## B. Governing equations and numerical methods

The above-mentioned DDT process was modeled by solving the 2D unsteady reactive Navier–Stokes equations, which are given by the following equations in conversation form:<sup>56</sup>

$$\frac{\partial U}{\partial t} + \frac{\partial(F_x - G_x)}{\partial x} + \frac{\partial(F_y - G_y)}{\partial y} = S_{chem}, \quad (1)$$

in which  $U$  denotes the vector of state.  $F_x$  and  $F_y$  represent the convection fluxes, and  $S_{chem}$  denotes the source term that gives by the mixture's chemical reaction.<sup>56</sup> These vector-valued quantities read

$$U = \begin{bmatrix} \rho_i \\ \rho u \\ \rho v \\ \rho E \end{bmatrix}, \quad F_x = \begin{bmatrix} \rho_i u \\ \rho u^2 + p \\ \rho uv \\ u(\rho E + p) \end{bmatrix}, \quad (2)$$

$$F_y = \begin{bmatrix} \rho_i v \\ \rho uv \\ \rho v^2 + p \\ v(\rho E + p) \end{bmatrix}, \quad S_{chem} = \begin{bmatrix} \dot{\omega}_i \\ 0 \\ 0 \\ 0 \end{bmatrix},$$

where  $u$ ,  $v$ , and  $E$  are the horizontal velocity, the normal velocity, and total energy, respectively.<sup>56</sup>  $\dot{\omega}_i$  are the mass generation rates of the species, which can be obtained from a specific chemical reaction mechanism of  $J$  as

$$\dot{\omega}_i = \sum_{j=1}^J (v_{ji}^r - v_{ji}^f) \left[ k_j^f \prod_{n=1}^{N_{sp}} \left( \frac{\rho_n}{W_n} \right)^{v_{jn}^f} - k_j^r \prod_{n=1}^{N_{sp}} \left( \frac{\rho_n}{W_n} \right)^{v_{jn}^r} \right], \quad (3)$$

$$i = 1, \dots, N_{sp}.$$

In the current simulation, only elementary chemical reactions were adopted. Therefore, the Arrhenius equation was employed to evaluate the reaction rates, which has widely been used in detonation simulations in previous work<sup>32,33,57</sup> and reads

$$k_j^{f/r} = A_j^{f/r} T^{\beta_j^{f/r}} \exp \left( -\frac{E_j^{f/r}}{RT} \right). \quad (4)$$

The chemical kinetics package CHEMKIN is employed to evaluate Eqs. (3) and (4) based on the specific chemical reactive mechanism.  $\rho$  in Eq. (2) denotes the total density, and  $i$  equals to 1, 2, 3, ...,  $N_{sp}$ , with  $N_{sp}$  denoting the total number of species. The total energy  $E$  is determined by

$$E = \sum_{i=1}^{N_{sp}} Y_i h_i - \frac{p}{\rho} + \frac{1}{2} (u^2 + v^2), \quad (5)$$

where  $h_i$  denotes the specific enthalpy of species  $i$ , and  $p$  is the ideal gas equation stemmed from the partial pressure equation for each species (see Ref. 56). The quantities  $G_x$  and  $G_y$  in Eq. (1) represent the diffusion fluxes obtained as

$$G_x = (\rho D_i \partial Y_i / \partial x, \tau_{xx}, \tau_{xy}, u\tau_{xx} + v\tau_{xy} - q_x), \quad (6)$$

$$G_y = (\rho D_i \partial Y_i / \partial y, \tau_{yx}, \tau_{yy}, u\tau_{yx} + v\tau_{yy} - q_y). \quad (7)$$

The shear stress terms in Eqs. (6) and (7) are determined by

$$\tau_{xx} = \mu \left( \frac{4}{3} \frac{\partial u}{\partial x} - \frac{2}{3} \frac{\partial v}{\partial y} \right), \quad \tau_{yx} = \tau_{xy} = \mu \left( \frac{\partial v}{\partial x} + \frac{\partial u}{\partial y} \right), \quad (8)$$

$$\tau_{yy} = \mu \left( \frac{4}{3} \frac{\partial v}{\partial y} - \frac{2}{3} \frac{\partial u}{\partial x} \right),$$

where  $\mu$  represents the mixture viscosity. The heat fluxes in Eqs. (6) and (7) are given by

$$q_x = -k \partial T / \partial x - \rho \sum_{i=1}^{N_{sp}} h_i D_i (\partial Y_i / \partial x), \quad (9)$$

$$q_y = -k \partial T / \partial y - \rho \sum_{i=1}^{N_{sp}} h_i D_i (\partial Y_i / \partial y), \quad (10)$$

where  $k$  and  $D_i$  are mixture-averaged thermal conductivity and mass diffusivities, respectively. The mixture dynamic viscosity  $\mu$  and the thermal conductivity  $k$  coefficients are modeled by the formulas of Wilke<sup>58</sup> and Mathur,<sup>59</sup> while the mass diffusion coefficients for averaged molecular species are modeled by a simplified equation that is inversely proportional to pressure. The thermodynamic and transport properties are calculated by the CHEMKIN-II package. Finally, Eq. (1) is closed by employing the perfect gas equation of state for each species. The above-mentioned equations were solved via AMROC (adaptive mesh refinement in object-oriented C++),<sup>51</sup> which has been extensively utilized for multi-dimensional detonation simulations.<sup>50,56,57,60–64</sup> The solver has also been successfully adopted for analyzing flame acceleration and DDT processes in previous research.<sup>16,47,62</sup>

A hybrid Roe–HLL (Roe–Harten–Lax–van Leer) Riemann solver<sup>51</sup> was employed for discretizing the upwind fluxes to potentially avoid unphysical total density and internal energy near vacuum due to the Roe linearization. The Minmod limiter with MUSCL (monotone upwind scheme for conservation laws) reconstruction was adopted to obtain second-order accuracy in space. A central difference scheme was utilized to handle the diffusion terms of the Navier–Stokes equations in Eq. (1). A semi-implicit generalized Runge–Kutta scheme with fourth-order accuracy was utilized for integration of the chemical

kinetics. For the chemical reaction source, the Godunov splitting with first-order accuracy was employed, and it has an enough accuracy compared to Strang splitting as reported by former study.<sup>51</sup> The level-set technique with ghost fluid approach<sup>65</sup> was introduced to implement the embedded solid wall boundaries when introducing the solid obstructions in the upper and lower walls, as highlighted by the yellow objects in Fig. 1.

In particular, a detailed chemical kinetic model of hydrogen–air<sup>66</sup> with 12 species and 42 elementary reactions was employed for modeling the chemical reaction for the flame acceleration and DDT processes. A comparison of Westbrook's and Burke's mechanisms<sup>67</sup> for the flame acceleration and DDT in case 1 was also conducted. The results demonstrate that the  $T_{DDT}$  for Burke's and Westbrook's mechanisms is  $t = 1.415\,43\text{ ms}$  and  $t = 1.375\,14\text{ ms}$ , respectively, which corresponds to just a 2.8% difference. The required  $L_{DDT}$  for the Burke and Westbrook reactive mechanism are  $L = 462$  and  $L = 505\text{ mm}$  so that the difference is 9.3%. The influence of the specific reaction mechanism on the current research appears to be small, and therefore, the Westbrook mechanism was primarily employed to simulate the DDT process throughout this study. It has also been employed in the previous study.<sup>47</sup>

### C. Mesh resolution test

An initial grid of  $L_x \times L_y = 1750 \times 50$  was employed as basic resolution with a maximum mesh size of  $4.0 \times 10^{-4}\text{ m}$  in both  $x$  and  $y$  directions. The AMR approach<sup>16,51,68</sup> was employed during the simulation of the entire DDT process. Three different refinements were taken into consideration to verify the effect of grid resolution on the flame acceleration. Consequently, the refined mesh size was reduced to  $1.0 \times 10^{-4}$ ,  $5.0 \times 10^{-5}$ , and  $2.5 \times 10^{-5}\text{ m}$  for the three meshes A–C, respectively. The laminar flame thickness for the present mixture given in Table I is  $L_1 = 3.5 \times 10^{-4}\text{ m}$ . As a result, three different refined levels were considered with 3.5, 7, and 14 grid points (Pts) in the laminar flame thickness (Pts/ $L_1$ ).

Case 1 in Table II was chosen as a physical model for the mesh resolution test. To reduce the computational cost, a limited computation time was considered to simulate the initial stage of the DDT process, and a higher initial pressure with  $P = 0.6\text{ MPa}$  in the hot spot with a radius of 10 mm was employed to trigger the flame acceleration. The obtained results of the flame propagation for the flame tip from

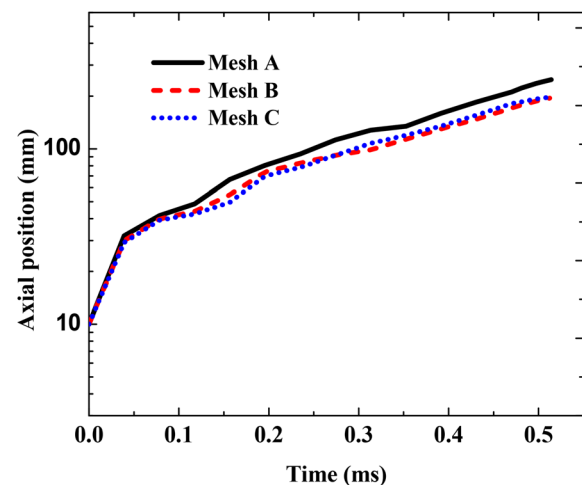


FIG. 2. Propagation of the flame front in the combustion tube for different mesh resolutions.

three meshes are illustrated in Fig. 2, where the vertical ordinate is scaled logarithmically. The simulations converge as the mesh resolution increases during the flame acceleration. As the mesh resolution increases, the locations of the flame front are almost collapsed into one as shown in Mesh B and Mesh C. As such, the mesh resolution in Mesh B is accurate to resolve the flame acceleration process properly, corresponding to 7 Pts/ $L_1$ . This result is in accordance with the literature where it was found that a mesh resolution from 5 to 10 Pts/ $L_1$  has little effect on the flame acceleration in the DDT simulation.<sup>14,16,32,40</sup> See especially Kessler *et al.*'s report<sup>40</sup> where the flame surface area has only a tiny difference between 5 and 10 Pts/ $L_1$  resolution.

It is found that the computing time (cpu  $\times$  h) for Mesh C almost requires four times that for Mesh A. Hence, it would take high computational resources for the high resolution in Mesh C when the flame propagates through the entire tube combustor. Consequently, since the current study does not emphasize the detonation wave propagation, the mesh resolution B corresponding to the level 4 refinement is adopted in the following flame acceleration and DDT studies to balance the computing requirements with accuracy in the current engineering simulations. The highest refinement factor is also applied on the upper and lower boundary walls. Adaptive results of AMROC for detonations<sup>7,56,57,68</sup> and DDT processes<sup>16</sup> were also validated in previous works. Hence, the AMR criteria are effective and robust in the current model to deal with the flame acceleration and DDT. The computations were carried out on the Tianhe-1 supercomputer located in the Changsha Computer Center, where 18 nodes with 216 cores were employed for simulating a single DDT process.

## III. RESULTS AND DISCUSSION

### A. Comparisons between flame acceleration and DDT

The flame front and temperature contours over time for the solid obstacles only (case 1 in Table I) are shown in Fig. 3. The mixture is ignited by a hot spot from the semi-circle [Fig. 3(a)]. The leading flame front propagates slowly at the initial stage but accelerates rapidly when it passes through the first solid obstacles with a velocity of 282 m/s at 0.47 ms [Fig. 3(c)]. The surface area of the propagating flame is

TABLE II. Different cases studied in the present work.

Case number	Study purpose	Jet position (mm)	Jet start time (ms)	Jet pressure (MPa)	Configuration
1	Comparisons of	...	...	...	A
2	both obstacles	100	0.001	0.35	B
3	Effect of dual jet	100	0.001	0.35	C
4	Effect of jet	100	0.25	0.35	B
5	start time	100	0.5	0.35	B
6		100	0.001	0.2	B
7	Effect of jet	100	0.001	0.5	B
8	pressure	100	0.001	0.65	B

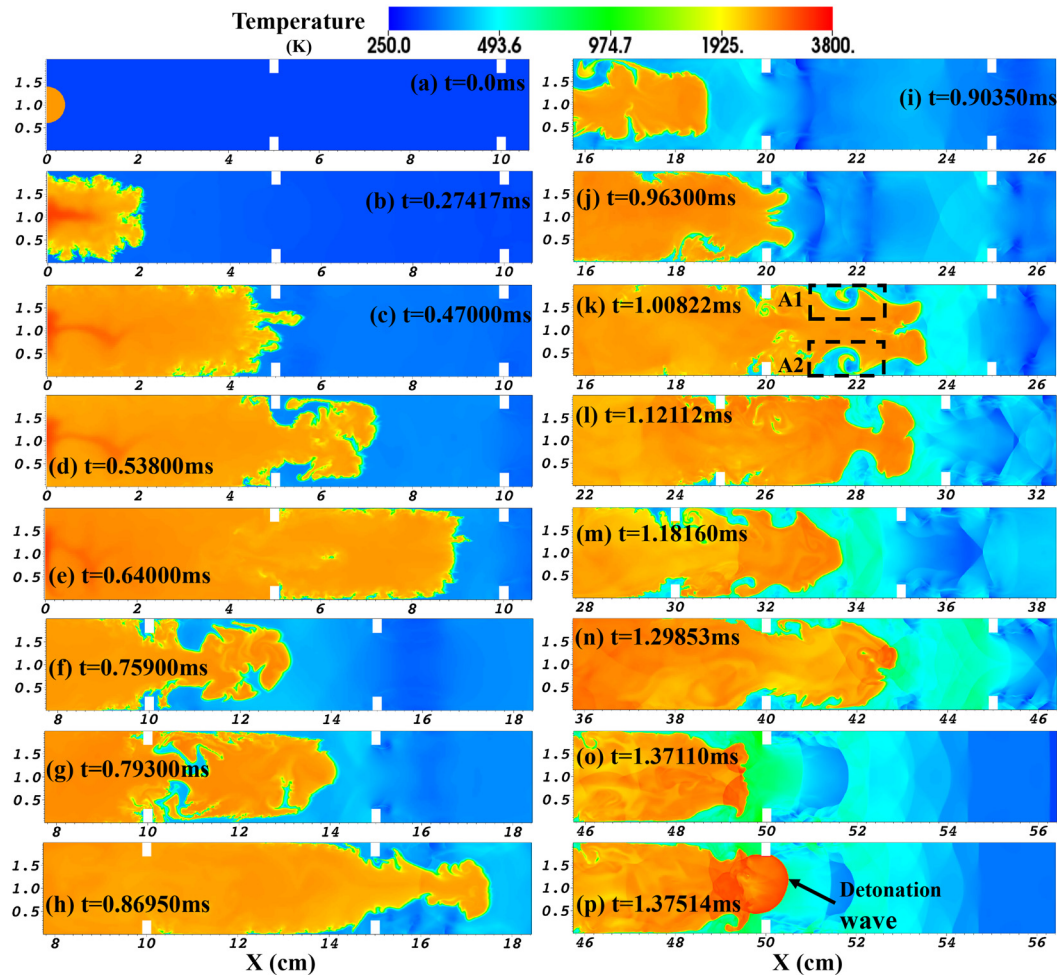


FIG. 3. Snapshots of temperature contours with time evolution for the entire DDT process that occurred in the combustion chamber with only solid obstacles (case 1).

dramatically wrinkled at  $t = 0.538$  ms [Fig. 3(d)], caused by the flow instability generated by the flow acceleration.<sup>30,32</sup> This results in an elevated surface area and instability of the flame front, which is mainly due to the high interactions between the turbulent flow and flame because of a series of instabilities including Rayleigh–Taylor (R–T) and K–H.<sup>14,33,40,53</sup> These further increase the energy release ratio as confirmed by previous research.<sup>32</sup> Simultaneously, the continuously increasing combustion flame introduces the compression wave, and the leading shock wave is subsequently generated when the compression waves focus together. The flame surface area is increasing dramatically when the flame front propagates into the recirculation zone and passes through the solid obstacles owing to the K–H and R–T instabilities, inducing two larger parallel eddies as marked in rectangles A1 and A2.

The flame goes into a deflagration stage, and the propagating velocity continues to be augmented to a magnitude of a half CJ velocity from  $t = 1.0082$  ms [Figs. 3(k) and 3(n)]. Consequently, the deflagration combustion produces a large number of complex shock waves that also induce a Richtmyer–Meshkov instability. The leading shock

wave heats the unburnt mixture before the leading flame front approaches, as seen in previous research.<sup>69,70</sup> The complicated interactions of the shock–shock, shock–turbulence, and shock–flame occur, leading to intense turbulent flow and pressure rise when there is a shock wave focusing.<sup>71</sup> Such features further lead to the occurrence of a local detonation starting at  $t = 1.37514$  ms [Fig. 3(p)]; hence, the DDT takes place successfully.

The occurrence of DDT requires ten pairs of solid obstacles. There is no doubt that it would be difficult to induce detonation combustion as an engineering application of a PDE when the ignition is started from the low-energy ignition. However, the requirement of detonation combustion triggered by a high-energy ignition is difficult for a discontinuous detonation engine because many solid obstacles placed in the combustion chamber also produce considerable propulsion loss, as discussed in the introduction. Therefore, the fluid obstacle is introduced into the combustion chamber. The obtained flow and temperature evolution as a function of time for case 2 are presented in Fig. 4. The initial stage of combustion is similar to case 1 from  $t = 0.0$  [Fig. 4(a)] to  $t = 0.64$  ms [Fig. 4(e)], where there is a large blockage of



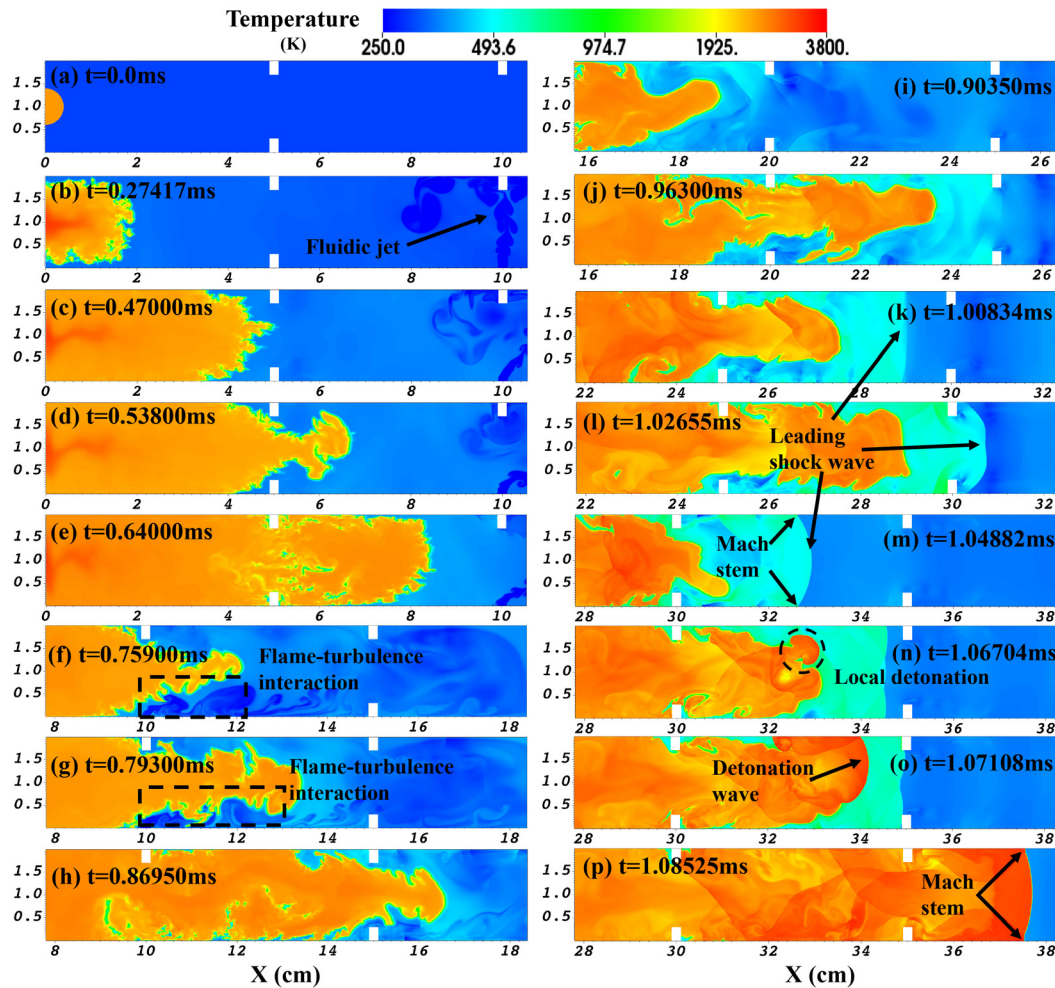


FIG. 4. DDT characteristics rendered by temperature in the combustion tube using the combined obstacles of the transverse jet and solid in case 2.

turbulent flow generated by the jet, as highlighted with lower temperature regions in Fig. 4(b). The crossflow deflection forms in the chamber because of the influence of the mainstream flow. Subsequently, the interaction between the flame and turbulence flow is formed clearly as marked by a black dashed rectangle at  $t = 0.793$  ms. The flame surface area increases significantly, enhancing the flame propagation velocity accordingly. Due to the intense flame acceleration, a shock wave and a preheated zone of the mixture between this shock wave and the flame front are also generated [see Figs. 4(k) and 4(m)]. Meanwhile, the intense leading shock wave is reflected from the bottom wall, forming a remarkable Mach stem at  $t = 1.048$  ms, promoting the detonation initiation.

The distance between the leading shock wave and the flame front is almost constant throughout this regime. These characteristics are called a pattern of “shock–flame” complex,<sup>25,30</sup> meaning that the flame velocity is almost the same as the leading shock wave. This stage also suggests that the detonation will be generated automatically in the region between the leading shock and the flame front. In particular, a localized explosion spot is formed, as denoted by a black dashed circle

in Fig. 4(n), where a higher temperature area is generated. This localized explosion further propagates downstream through the chamber, generating an overdriven detonation. Meanwhile, the flame front is mostly spherical. This is due to the onset of detonation in DDT scenarios being overdriven, which is less cellularly unstable as the ratio of the overall activation temperature to the leading post-shock temperature is reduced. The subsequent Mach stem is generated, enhancing the detonation combustion [see Fig. 4(p)].

The detailed variations of the temperature and pressure contours before and after the detonation initiation are illustrated in Fig. 5. As the two reflected shock waves [see arrow SW1 and arrow SW2 in Fig. 5(a1)] collide together, a hot spot with increasing pressure, as highlighted by the red dashed circles B1 and B2, is formed [Figs. 5(a2) and 5(b2)]. The maximum pressure value of the spot reaches 9.20 MPa, which is almost six times that of the theoretical CJ pressure. Therefore, the mixture in this spot is preheated due to the intense reflected shock wave focusing. Meanwhile, the reaction front of the flame also interacts with the high-pressure spot region as denoted by the black dashed circle in Fig. 5(b1). Consequently, a localization

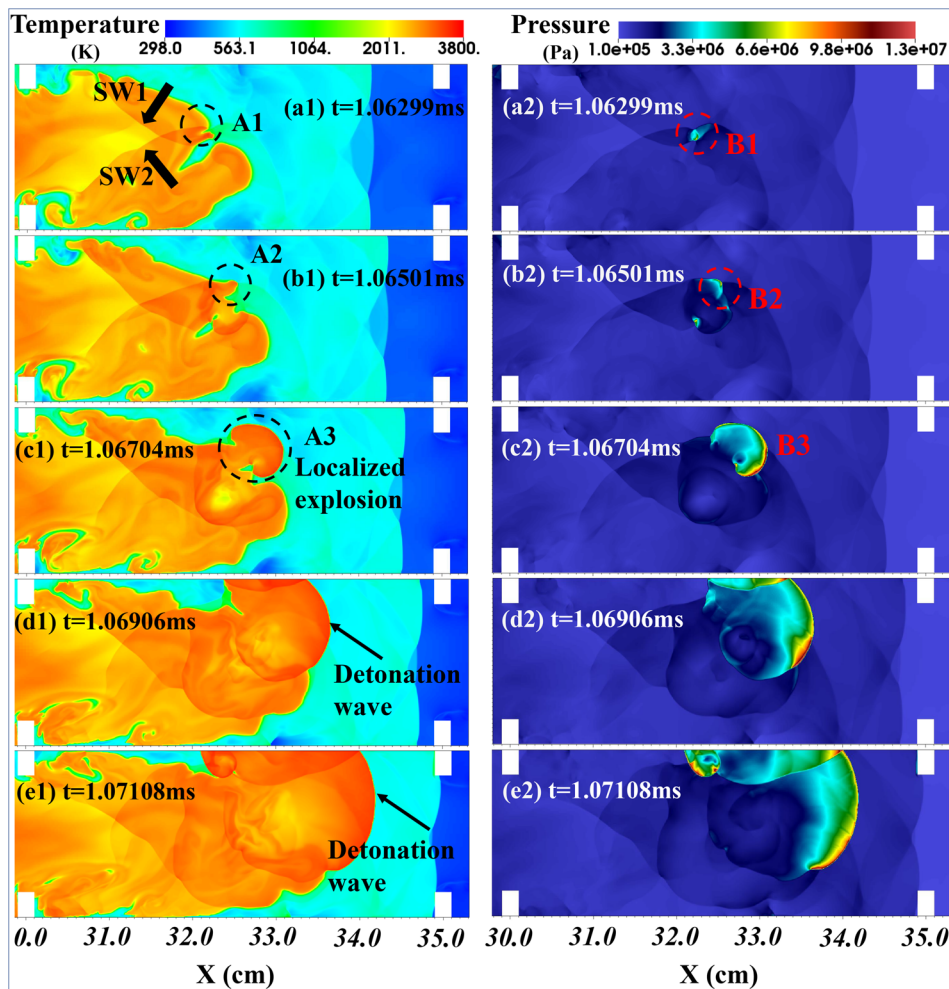


FIG. 5. Temperature (left) and pressure (right) color plots for different times before and after the occurrence of detonation. SW—shock wave.

explosion region induced by these factors is formed [see Fig. 5(c1)], resulting in a detonation transition. This DDT mechanism is attributed to rapid energy deposition in a small localized region on a quite small timescale. This onset of detonation is also observed in the numerical result of Goodwin *et al.*'s study<sup>53</sup>. This detonation transition is a typical DDT mechanism in a low Br configuration, which is often formed by a spot that has high pressure and high temperature before direct initiation generated by the shock wave focusing. The current ignition mechanism always takes place in a condition where there is a slightly large spatial interval (S in Fig. 1) between the solid obstructions. It is also consistent with direction initiation theory,<sup>72</sup> as reported in experimental research for a low Br.<sup>73</sup> After that, the overdriven detonation wave expands to the downstream chamber as shown at  $t = 1.07108$  ms.

The pressure records along the central line of the chamber varying with time for case 2 are further superimposed on Fig. 6. As shown, the pressure gain is produced by the gas expansion in the left side region of the tube at  $t = 0.31333$  ms. Note how two parallel regions, that are lower than the initial charge pressure, are formed, which is attributed to the transverse jet that produces lower pressure regions.

The pressure in the left side of the tube continues to be augmented as the mixture burns out with a higher energy release ratio, which can be proved by the red arrow A in Fig. 6(a). Subsequently, the compression wave is generated in the combustor as a result of the response of the thermomechanical energy caused by the elevated energy release ratio,<sup>15</sup> and it further propagates along the tube (see  $t = 0.8015$  and  $t = 0.9035$  ms). In addition, there is a high fluctuating pressure due to the reflected shock wave propagating from the upper and lower walls, or the solid obstacles.

The pressure continues to be increased from  $P = 1.2$  to  $P = 2.0$  MPa, as shown by the maximum point at  $t = 1.0$  and  $t = 1.041$  ms, feeding back to heat the unburned material and creating a condition that induces the detonation initiation. Hence, the leading shock wave incorporated in the flame front evolves into a detonation wave, resulting in a high-pressure difference between the induced reaction zone and fresh mixture, as illustrated at  $t = 1.091$  and  $t = 1.144$  ms. The detonation combustion is still in a stage of overdrive. Hence, its pressure is higher than the CJ value.<sup>74,75</sup> It is worth mentioning that the pressure ratio in the current tube combustor is still close to the range of 15–20 across the detonation wave, as confirmed



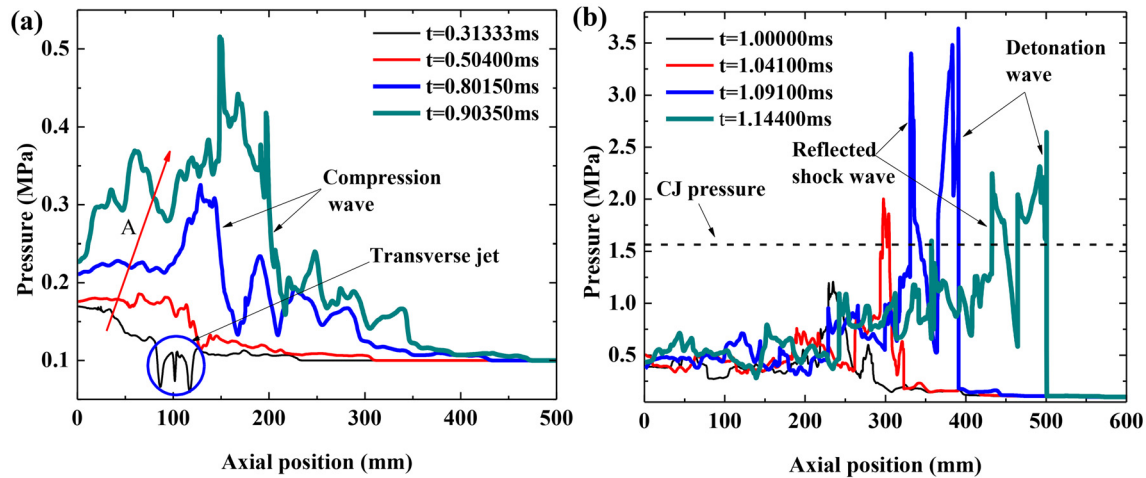


FIG. 6. Pressure records along the central line of the chamber for case 2, (a) initial stage of combustion; (b) stage around the detonation occurrence.

by previous research. It is around twice that produced in the deflagration combustion under the almost constant volume conditions.<sup>2,6</sup>

To clearly picture the variations of the flame tip in both cases, comparisons of the flame front and the corresponding flame front propagation velocity with time evolution for cases 1 and 2 are plotted in Figs. 7(a) and 7(b), respectively. At the initial stage, the flame tip that takes place in case 1 is slightly higher than that in case 2, indicating that the flame propagation velocity in case 1 is larger than that in case 2, which is confirmed by the incipient stage of velocity variation in Fig. 7(b). This is caused by the later transverse jet that introduces a high Br around  $t = 0.538\,00\text{--}0.640\,00\text{ ms}$ , which generates a high-pressure region and blocks the initial propagation of the flame slightly before the flame tip approaches the jet exit, whereas the axial position of the flame front in case 2 catches up with case 1 after around  $t = 0.9\text{ ms}$ , as demonstrated in the zoomed view of Fig. 7(a). The latter

is attributed to the flame–turbulence interactions during the state from  $t = 0.759\text{ ms}$  [Fig. 4(f)] to  $t = 0.903\,5\text{ ms}$  [Fig. 4(i)], leading to an increasing flame surface area that increases the flame propagation velocity, as identified by the blue dash circle in Fig. 7(b). Such an increased flame surface area produced by the flame–turbulence interactions was also observed in previous numerical simulations in a smooth chamber and experimental investigations at the early stage of the transition from the laminar flame to turbulent flame.<sup>43,44</sup> After  $t = 0.9\text{ ms}$ , the axial flame position in case 2 is gradually higher than that in case 1.

Figure 7(b) presents a typical flame front velocity variation during the flame acceleration and DDT processes. The flame propagation velocity increasingly fluctuates from almost zero to a velocity that is higher than the theoretical CJ value, implying that the transition from deflagration to detonation has occurred. The initial detonation is

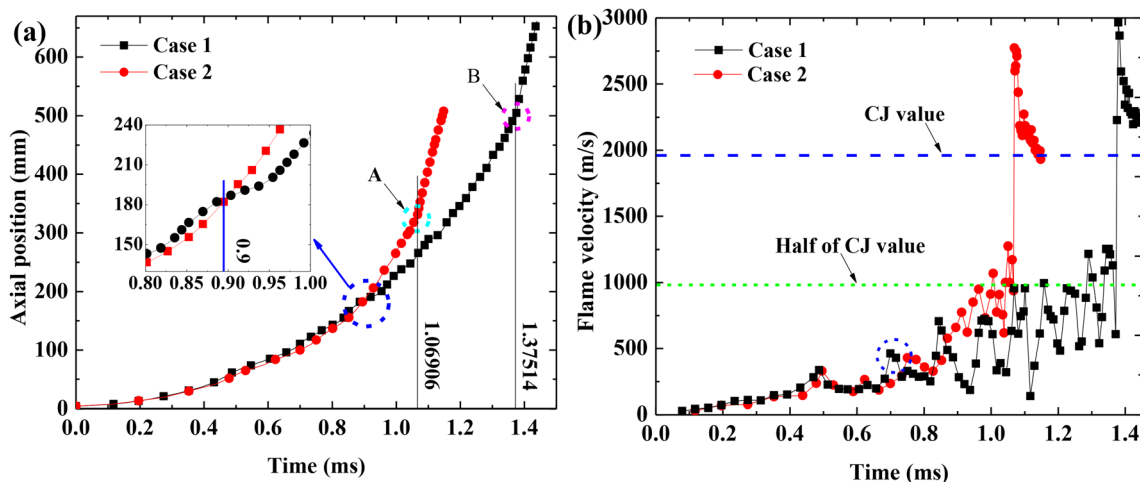


FIG. 7. (a) Axial position of the flame front and (b) the flame front velocity vs time for the chamber with solid obstacles only case 1, and the case with combined fluid and solid obstacles (case 2).

**TABLE III.** The obtained  $T_{DDT}$  and  $L_{DDT}$  for the onset of detonation for cases 1 and 2.

	Case 1	Case 2	Enhanced efficiency (%)
DDT run-up time (ms)	1.375 14	1.069 06	22.26
DDT run-up distance (mm)	505	336.55	33.36

almost an overdriven detonation during the incipient DDT process.<sup>6,30</sup> Subsequently, the flame velocity decreases gradually for both cases and approaches the theoretical CJ value, suggesting that the detonation enters a stable state. There is an apparent velocity difference after the occurrence of detonation, and the magnitude of the deflagration velocity is almost half the CJ value. Hence, a propagating flame speed of about half the theoretical CJ value is required before the occurrence of detonation. This is because there is no continuous transition from the deflagration combustion in the lower branch to the detonation model in the upper branch associated with the Hugoniot curve,<sup>31</sup> derived from the theoretical solution. This observation is also consistent with recent experimental and numerical research on the DDT process.<sup>33,49,53,75</sup> Moreover, this rule is a rough criterion only, and the onset of detonation also depends on the obstruction and lower values (40% CJ speed) can be sufficient.<sup>75</sup> In terms of the stage before the detonation, there is a high fluctuating velocity for the propagating flame, which contributes to the influence of the solid obstruction. A more detailed discussion associated with these deflagration mechanisms in both cases will be given in Sec. III B.

The above-obtained results of the  $T_{DDT}$  and  $L_{DDT}$  for cases 1 and 2 are listed in Table III, which can be obtained from Fig. 7(a) as

marked by Points A and B. The  $T_{DDT}$  is shortened from  $t = 1.375\ 14$  to  $t = 1.069\ 06$  ms when employing a single transverse jet; hence, there is a 22.26% improvement in the  $T_{DDT}$ . In addition, the  $L_{DDT}$  is also shortened from  $L = 505$  to  $L = 336.55$  mm so that the improvement reaches 33.36% compared to the chamber only having solid objects, meaning that the required number of solid obstacles can be reduced from 10 to 7 pairs. Furthermore, the reduced time and length of the DDT process further suggest that the performance of a PDE would be elevated due to its high operating frequency.

## B. The mechanisms of flame acceleration in combined obstacles

For revealing the mechanisms of the combined obstacles on the flame acceleration, further detailed information involved in the combustion evolution and flame–turbulence interactions for cases 1 and 2 are given in Fig. 8 before  $t = 0.9$  ms. These snapshots are rendered from the density, where the black regions represent the combustion product due to the lower density, while the much higher density denotes the mixture downstream of the transverse jet. At  $t = 0.64$  ms [Fig. 8(a1)], the flame fronts of both cases are almost the same. The flame penetration is formed in case 1 in Fig. 8(b1). Next, the surface area of the flame continues to increase, resulting in a high-energy release ratio from the mixture that further augments the propagation velocity in case 1. As a consequence, the baseline A in case 1, constructed from the flame tip at different times, has a large slope compared to that in case 2 at the incipient stage. However, the surface area with no conspicuous distortion decreases within the chamber in the range of  $5 < X < 10$  cm in Fig. 8(e1) due to the increasing volume of the chamber when there is no obstruction. Yet, it undergoes the next acceleration due to the decrease in flow area caused by the paired solid

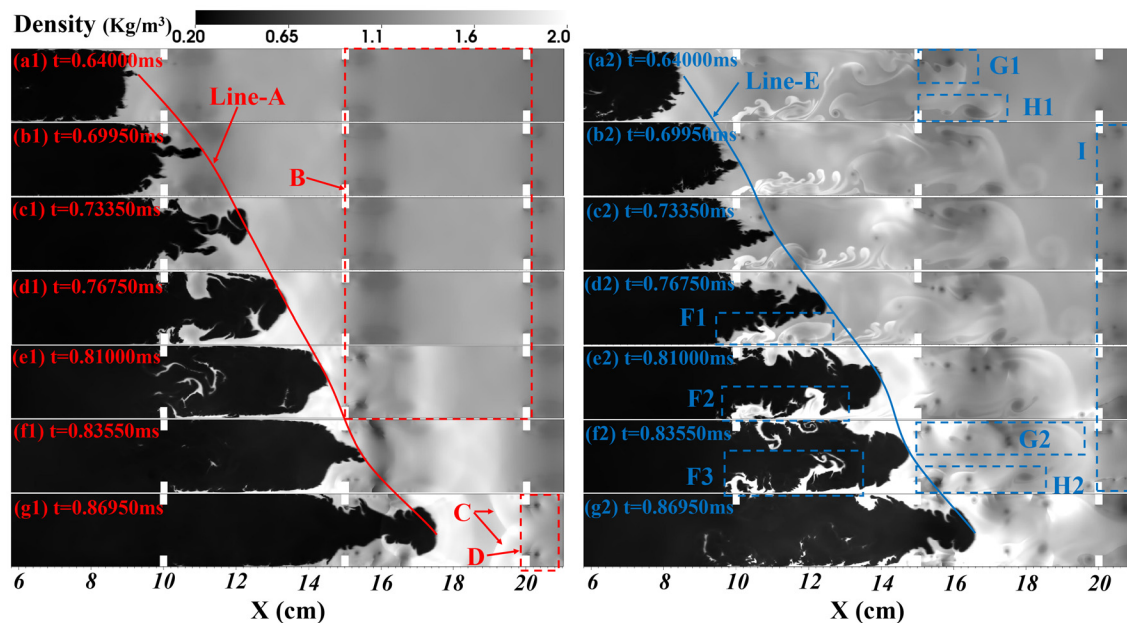


**FIG. 8.** Snapshots of density distribution in the downstream chamber during the initial time and before the occurrence of DDT (the left column is the chamber only having solid obstacles in case 1, while the right column is the combined fluid and solid obstacles in case 2).

obstructions at  $X = 15$  cm. The reflected compression wave is formed as denoted by arrow C. Meanwhile, the small vortices shedding from the tip of the solid obstruction are generated in the red dashed box D.

In terms of combined obstacles in case 2, the flame penetration occurs later, and it persistently continues from  $t = 0.7335$  ms to  $t = 0.81$  ms. This is due to the gradual decrease in the free flow area of the flame, which is partially occupied by the transverse jet, as shown in Fig. 8(d2), leading to the flame acceleration. In addition, the flame front is far away from the tip of the solid and the outer boundary of the transverse jet and almost has a symmetry structure along the central line of the chamber, as shown in Fig. 8(c2). This is attributed to the accumulation of a high-pressure region ahead of the combined obstructions from the solid plate and transverse jet. It indicates that the transverse jet obstacle can play the same role as a solid obstruction. The large turbulent eddies stemming from the exit of the transverse jet are formed by the influence of the mainstream fluid flow. Next, the outer shear layer introduced from the jet stream interacts with the lower flame front, yielding a conspicuous deformation, deflection, and recirculation flow of the flame tip, as indicated by the rectangles F1, F2, and F3, which further augments the flame surface area, producing a persistent flame acceleration.

Further inspecting the downstream flame front in the same region, as denoted by a red dashed box B, it can be found that there is a dramatic difference. No prominent turbulent flow forms in case 1; conversely, remarkable turbulent flow penetration and eddies are observed, and these turbulent flows interact with the fixed solid obstructions, producing a large block of K–H instabilities from the tip of the solids, which gradually propagate downstream the channel. It also expands the influential regions with time evolution, as indicated by the blue dashed boxes G1 and H1 to G2 and H2. A lot of K–H instabilities are generated at an early stage as shown by the blue dashed box I in case 2. These flow characteristics will influence the upcoming flame front [see Fig. 8(g2)]. Recent works<sup>16,76</sup> have conducted detailed research of the transverse jet on the DDT process in a smooth channel, and the results demonstrated that there are a lot of mushroom vortices in the jet exit downstream, but no significant K–H instabilities can be formed in the downstream tube.

To compare the flame propagation differences in cases 1 and 2, Fig. 9 provides the variations of velocity, vorticity, and pressure contours, where the black line within these contours represents the flame front, which was extracted from the OH elementary contour. A high-velocity region appears in the penetration flame front in the red

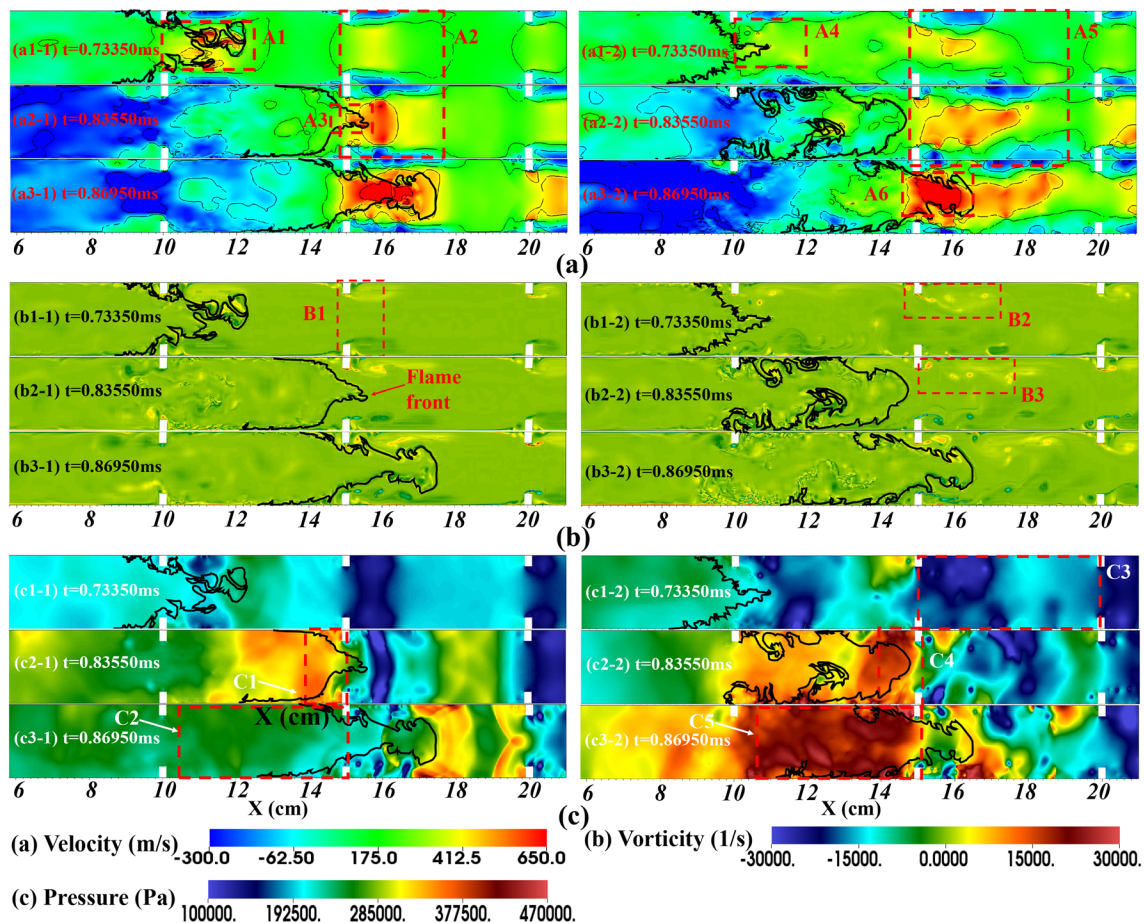


FIG. 9. Time evolution of (a) velocity, (b) vorticity, and (c) pressure contours during the flame propagation for two cases; the left side is case 1, while the right side is case 2.



rectangles A1 and A3 in case 1 and the red box A4 in case 2. However, the flame propagation velocity decreases when the flame tip propagates into the separated interval between the obstructions in case 2 [see Fig. 9(a2-2)].

Moreover, there is almost a symmetric distribution of velocity along the central line of the tube as shown by box A2, while a more non-uniform distribution of velocity contour is generated because of the transverse jet influence (see box A5 in case 2). This region has a higher velocity than that in case 1 at the same time. Hence, it can be concluded that the transverse jet stream can significantly influence the downstream flow field. A high magnitude of fluid flow with non-uniform distribution can be formed early ahead of the upstream flame front.

The flame–turbulence interactions can be further evidenced by the vorticity contours. The jet in crossflow mainly forms a large part of clockwise (negative) vorticities under the influence of the mainstream flow, which prompts the turbulent reactant transport when the flame front approaches the outside boundary layer of the transverse jet [see Fig. 9(b2-2)]. A large part of anti-clockwise (positive) vorticities is generated, and it is growing from the tip of solid obstruction from boxes B2 to B3 in case 2. These vorticities evolve into large turbulent vortexes at the next time and enhance the turbulent reactant transport when the flame front propagates in those regions.<sup>43,44</sup> By contrast, just a few vorticities with lower magnitude are gradually forming due to the K–H instability (see box B1).

The lower pressure regions are formed behind the solid objects, as shown by box A1 associated with case 1. The pressure increase is formed as marked by box C1 in case 1 due to the Br.<sup>14,32</sup> As such, the flame front is wrinkled and stretched. Regarding case 2, the non-uniform distribution of pressure contour in box C3 is generated because of the large turbulent flow and eddies, as proved by Figs. 9(b). The high asymmetry pressure spots are generated in the red dashed box C4, deflecting the flame front later. Moreover, there is a high-

pressure region in the unconfined space between  $10 < X < 15$  cm (boxes C4 and C5) in the same regions, resulting in a higher flame acceleration in case 2.

The next flame propagation rendering from temperature for both cases after  $t = 0.9$  ms is shown in Fig. 10. The baseline A established from the flame front in case 1 has a lower slope from Figs. 10(a1) to 10(d1). In contrast, there is a high slope of line B in case 2 due to the different flame acceleration ratios. A flat flame front is formed before the solid obstruction at  $X = 20$  cm thanks to the Richtmyer–Meshkov instability<sup>77</sup> caused by the reflected wave. On the other hand, a penetration flame front is generated as shown by the black dashed box A caused by the flame–turbulence interactions. The flame front is further wrinkled and stretched by the turbulent vortexes generated by the transverse jet at the last stage visualized by Fig. 9(b). These characteristics stimulate the increase in the flame surface area; hence, an abrupt energy release ratio introduces a high flame acceleration.<sup>32,33,53</sup>

To further reveal the flame propagating mechanisms in case 2, Fig. 11 presents the evolution of pressure, vorticity, and velocity vector at the same time with Fig. 11(b). An increasing pressure region appears in the top boundary ahead of the solid object (see boxes A1 and A2) due to the flame deflection, which contributes to the negative vorticity influence, as shown by boxes B1 and B2. These vorticities further deflect the flame front and form remarkable flame–turbulence vortexes, as demonstrated by the rectangles B3 and B5. Subsequently, the high-pressure region appears in box A2 and the low-pressure region shown in box A3 is further deflecting the flame tip, as shown in box B4, yielding a stretched flame front, then increasing the flame surface area. These combined influences act on the flame front resulting in continuously increased velocity when the flame tip crosses a confined area, as confirmed by the high magnitude of the velocity vector marked by boxes C1–C4.

For the purpose of quantitatively revealing the mechanisms of flame acceleration, Fig. 12 presents the temporal flame tip propagation

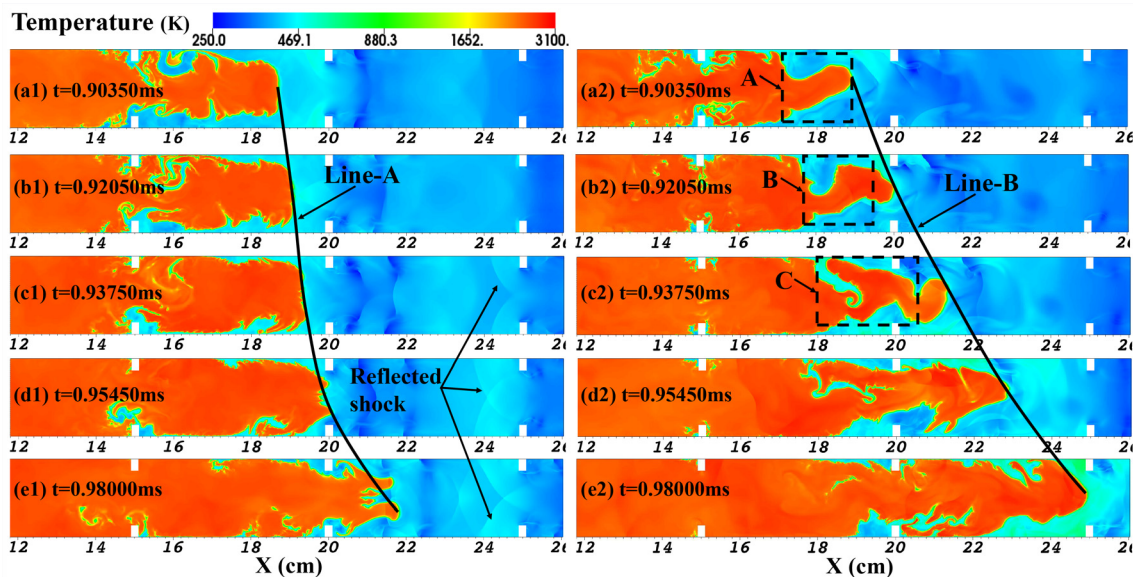


FIG. 10. Time record of temperature contours with the flame propagation for cases 1 (left column) and 2 (right column).

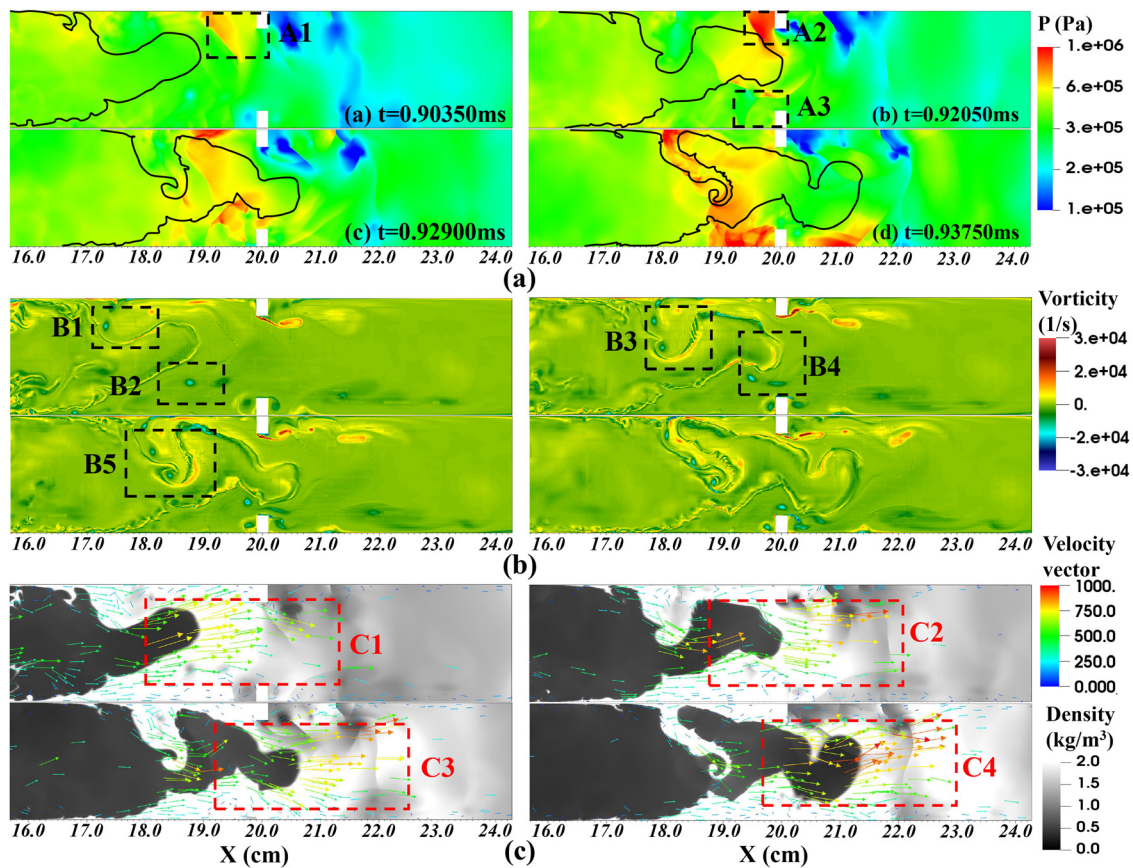


FIG. 11. Variations of the flame propagation downstream of the transverse jet in case 2 (the upper row is the (a) pressure contour; the middle rows are the (b) vorticity contours; while the lower row is the corresponding (c) velocity vector; and the background is the density contour).

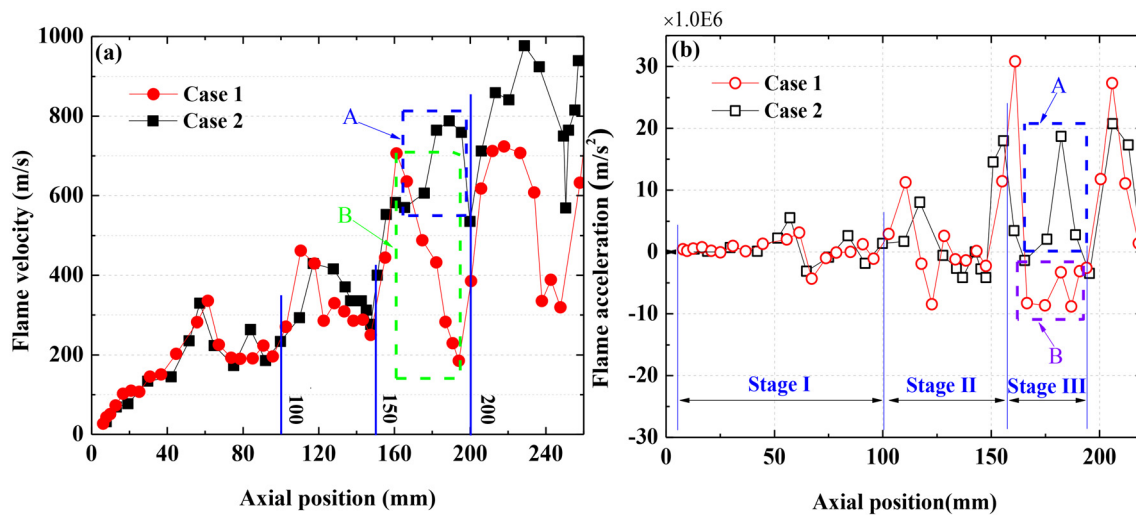


FIG. 12. Comparisons of flame front propagation velocity (a: left plot) and the acceleration ratio with time evolution (b: right plot) for cases 1 and 2. (a) The variations of propagating flame velocity and (b) the variations of transient acceleration.



velocity and the corresponding acceleration of flame spreading along with the axial position of the channel at the incipient stage for cases 1 and 2. The variations for both variables can be categorized into three stages. In stage I, the profiles in both cases have almost the same trend ahead of  $X < 100$  mm because the configuration at the front tube is the same and there is yet no noticeable influence from the downstream transverse jet in case 2. In stage II, the flame velocity for case 2 is higher, then lower than that in case 1. This is due to the jet influence, which initially provides a high Br that has a negative effect on the flame front propagation, then produces an intense flame–turbulence interaction that increases the surface area. These interactions can also be observed in boxes F1–F3 (see Fig. 8). As a result, an initial increase, then a sudden decrease in the flame acceleration is observed at stage II in Fig. 12(b). Then, the flame front experiences the next acceleration under the paired solid obstructions at  $X = 150$  mm. Both cases have an abrupt increase in flame speed around the barrier, resulting in a sharp increase in the flame acceleration. However, a quick decrease in the flame velocity in case 1 occurs in box B because of the increase in flow area as discussed above. Conversely, a preserved increase with no obvious decrease in the flame velocity in case 2 is observed as denoted by frame A. This is because of the turbulent vortices influence in the current stage as discussed in Fig. 11. After these complicated flame accelerations, the speed is further accelerated to a scale of half CJ value (1000 m/s) in the next acceleration stage III in case 2 as demonstrated in Fig. 12(a). Consequently, the combined obstacles in case 2 result in a shorter run-up time and less run-up distance of the occurrence of the DDT. Almost the same value of flame propagating velocity (700 m/s) is generated in the next accelerating stage associated with case 1, which will require more run-up time and run-up distance to accelerate the flame speed into a magnitude of one-half of the CJ speed.

In summary, the main results demonstrate that the jet obstacle plays a similar role for the Br as the solid obstacle when the flame front passes the upper jet position. In addition, the early flame–turbulence interactions ahead of the jet exit presented in Fig. 8 result in the flame deflection and a significant augment of the flame surface area, forming a remarkable pressure gain combustion as proved by the pressure contour in Figs. 9(c2-2) and 9(c3-2). Furthermore, the early transverse jet under the effect of mainstream flow introduces more intense turbulent flow and eddies that interact with the fixed obstacles, producing a lot of K–H instabilities shedding from the solid plates compared to that with only solid obstacles in case 1, as demonstrated by the vorticity contours in Figs. 9(b2-1) and 9(b2-2). Subsequently, these characteristics introduce further flame–turbulence interactions that curve and stretch the flame tip as shown in Figs. 9(a2)-9(c2); therefore, a persisted flame acceleration without conspicuous decrease is formed, as confirmed by the record of flame velocity in Fig. 12(a). These main outcomes lead to the propagating velocity of the flame front in case 2 reaching about half of the theoretical CJ velocity and promoting the onset of detonation.

### C. The effect of head-on jets on the flame acceleration and DDT

For further revealing the flame–turbulence interactions that have a positive effect on shortening the  $T_{DDT}$  and  $L_{DDT}$ , the dual jets in crossflow placed in the chamber are investigated here, as demonstrated by configuration C in Fig. 1(c). The evolution of the head-on jet stream and the flame acceleration rendering from density and the subsequent DDT process are presented in Figs. 13(A) and 13(B),

respectively, corresponding to case 3 in Table II. As shown in Fig. 13(A-a), two mushroom vortices propagate upstream and downstream along the axial direction, due to the head-on impact of the jet. Then, the leading mushroom eddies propagate anti-clockwise and clockwise along with the chamber. Under the effect of the mainstream, the jet stream is perturbed; then, the disordered and intense vortexes are formed accordingly [Fig. 13(A-c)]. More turbulent flows and eddies are generated in the downstream chamber compared to case 2 at the same time of  $t = 0.64$  ms. Meanwhile, the leading mushroom vortex in the upstream tube interacts with the leading flame front, as denoted by arrows A and B. This flame–turbulence interaction further propagates, forming a slim and stretched flame front as denoted by boxes B1–B4 in Fig. 13(A). This interaction enlarges the flame surface area dramatically, resulting in a high propagation velocity of the flame. The turbulent flow interacts with solid obstacles, resulting in triggering the K–H instabilities. As such, as shown in box C, more regions of turbulent flow in the downstream tube are observed. These outcomes further result in a high flame propagation velocity. Subsequently, a shock–flame complex feature is generated as shown in Figs. 13(B-m)–13(B-o). As a result, a localized explosion is activated at the bottom wall boundary, and it further expands to the downstream chamber, leading to a significant detonation wave and Mach stem with a shorter  $T_{DDT}$ .

The propagation of the flame front and the corresponding velocity for cases 1–3 are compared in Figs. 14(a) and 14(b), respectively. The flame front in these three cases almost collapses into one. However, as more transverse jets are injected into the chamber, the velocity of the flame front increases abruptly (see circle A). The  $T_{DDT}$  in case 3 is shortened by about 28.72% compared to that in case 1 with solid obstacles [Fig. 1(a)]. The  $L_{DDT}$  in cases 2 and 3 is almost the same, but an 8.15% decrease in the  $T_{DDT}$  in the head-on jet stream is obtained compared to that in the single jet and solid obstacles (case 2).

### D. The effect of initial time of jet on the flame acceleration and DDT

The start time of the transverse jet after the ignition of the mixture is studied. Cases 4 and 5 are employed here, corresponding to  $t = 0.25$  and  $t = 0.5$  ms to detect the downstream turbulent flow effect on the DDT process. The evolution of the flame front and transverse jet penetration at the initial stage and the subsequent flame acceleration is presented in Fig. 15 for case 4. A conspicuous deflection is formed in the chamber after the jet is injected into the channel due to the mainstream flow influence and the delayed start time of the transverse jet; as such, no visible turbulent flow is formed ahead of the exit of the jet. However, there is still enough distance between the jet exit and the current flame front. Consequently, the intense turbulent vortexes are gradually formed at the downstream tube before the flame front reaches the transverse jet exit. The fluid is only propagating along the lower boundary wall owing to the increasing mainstream flow, and the K–H instability is occurring and shedding from the tip of solid objects at  $t = 0.691$  ms (Fig. 15(c)). Nevertheless, the influence region generated by turbulent flow is less than that in case 2 due to the less jet flowing into the chamber. Next time, similar outcomes of flame–turbulence interactions with case 2 also appear in Fig. 15(d), introducing a stark increase in the flame surface area. After experiencing a series of flame accelerations, a strong leading shock wave is generated, forming a Mach stem within the obstruction interval in Fig. 15(g). Hence, overdriven detonation combustion with a

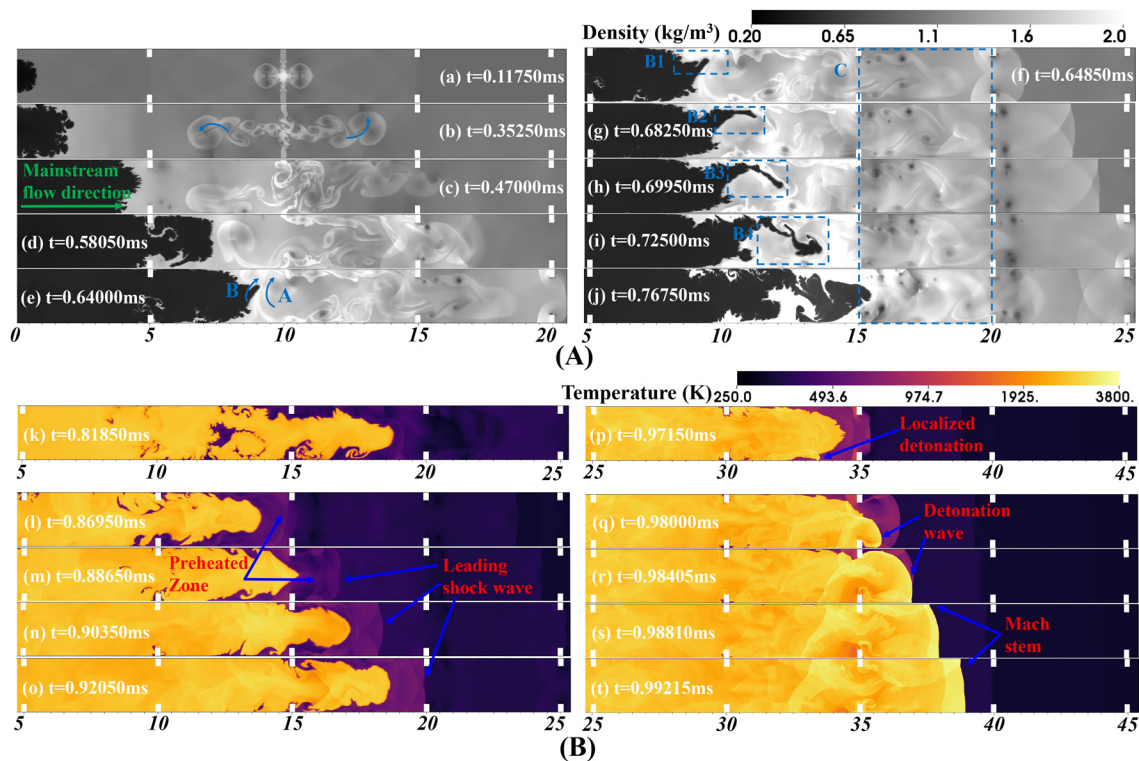


FIG. 13. The density contour and the subsequent flame front vs with time for case 3 [the upper row is (A) density contour, and the lower row is (B) temperature contour].

higher temperature occurs in this preheated zone ahead of the solid objects at  $t = 1.2218$  ms.

Figure 16 also presents the snapshots of flame propagation and flame–turbulence interactions rendered from density at the early stage and temperature contours at the next stage, respectively, for case 5. Just a tiny jet is injected into the chamber, and the transverse jet is

directly deflected by the mainstream flow. Consequently, a small influence region that disturbs by the transverse jet is introduced. The transverse jet stream is stretched along the bottom wall as shown in Fig. 16(b). No obvious curved flame front is generated as shown in Figs. 16(c) and 16(d). The transverse jet with a delayed start time has just the same function as a fixed solid obstruction. Subsequently, the

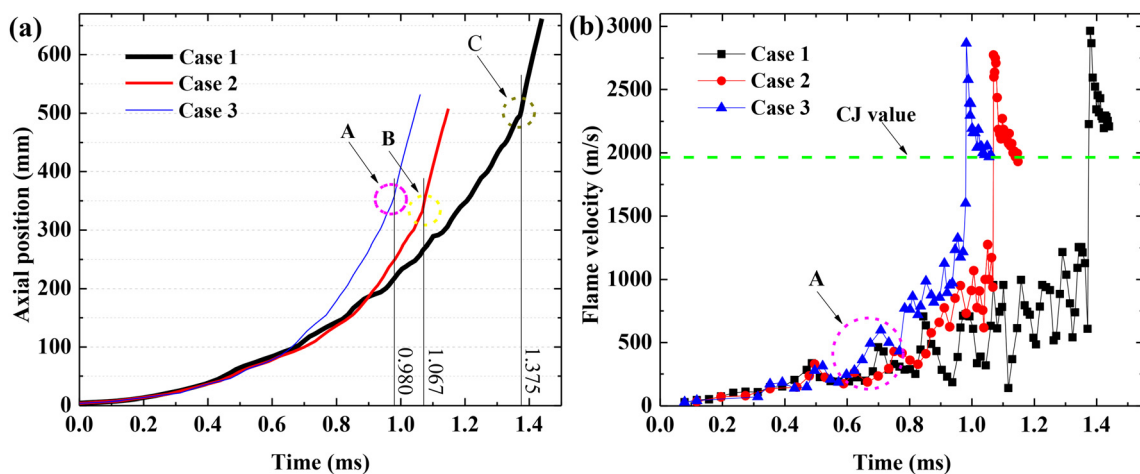
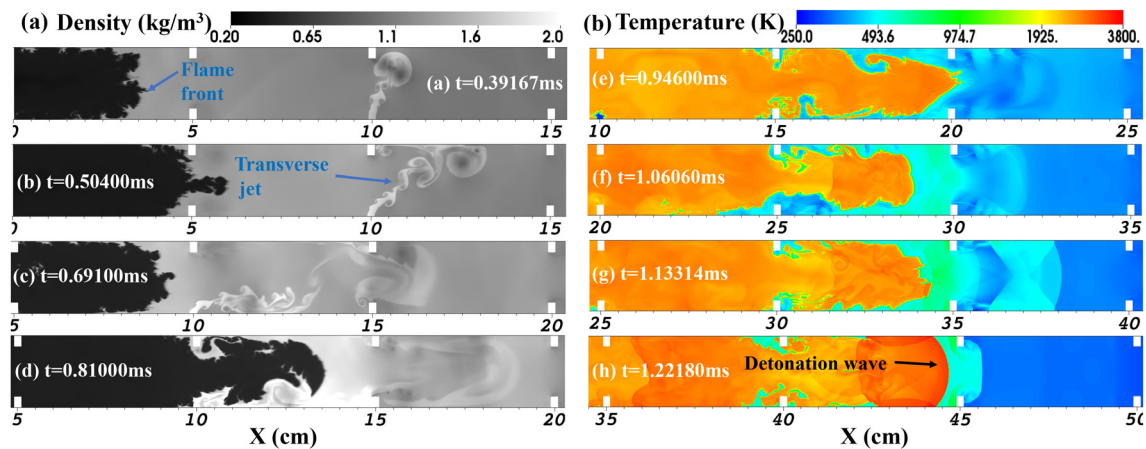


FIG. 14. (a) Axial position of the flame front and (b) velocity vs time for different flame acceleration methods (case 1: solid obstacles; case 2: single jet and solid obstacles; case 3: dual head-on jets and solid obstacles).



**FIG. 15.** The propagation of density contour at the initial stage and the subsequent flame front evolution for case 4 [the left column is (a) density contour, while the right column is (b) temperature contour].

flame propagation nearly experiences the same processes as in case 1, including the wrinkled flame and enlarging of the surface area caused by the recirculation flow and shock–flame interaction as presented by the series of snapshots in Figs. 16(e)–16(g). The DDT is activated by the same preheated region between the leading shock wave and flame front.

Variations of flame front position and flame front propagating velocity with time for cases 2, 4, and 5 are plotted in Figs. 17(a) and 17(b), respectively. The detonation combustion is formed in all cases successfully in a limited length of the tube, as denoted by the corner point by points A–C in Fig. 17(a). The  $T_{DDT}$  for cases 2, 4, and 5 are  $t = 1.067$ ,  $t = 1.218$ , and  $t = 1.347$  ms, respectively. Hence, there is an improvement of 20.79% of  $T_{DDT}$  in case 2 compared to that in case 5, whereas for cases 4 and 5, although the detonation initiation in case 4 is faster than that in case 5, the  $L_{DDT}$  in both cases are almost the same. The strength of flame–turbulence interaction in case 4 is more intense than that in case 5, caused by the additional jet stream

injection into the chamber in case 4, resulting in a preserved propagation velocity.

As shown in Fig. 17(b), the propagation velocity of the flame front for cases 4 and 5 is almost similar to case 2 at the initial stage, while with more fluids injected into the chamber,  $T_{DDT}$  is reduced. Additionally, the flame velocity variations gradually decrease to the theoretical CJ value after the occurrence of the DDT. Such feature is attributed to the fact that the overdriven detonation generated at the initial time gradually falls into a stable detonation, which is in accordance with the previous experimental and numerical research.<sup>16,32,75</sup> Furthermore,  $T_{DDT}$  in cases 1 and 5 is almost the same, corresponding to  $t = 1.3745$  and  $t = 1.347$  ms, respectively. Hence, the transverse jet in case 5 almost plays a single role as a solid obstacle. In general, it can be concluded that the start time of a transverse jet with an early operation is conducive to flame acceleration. With the increase in the delay time of jet operation after the mixture ignition, the transverse jet is changed from two functions that form a suitable Br and produce a lot

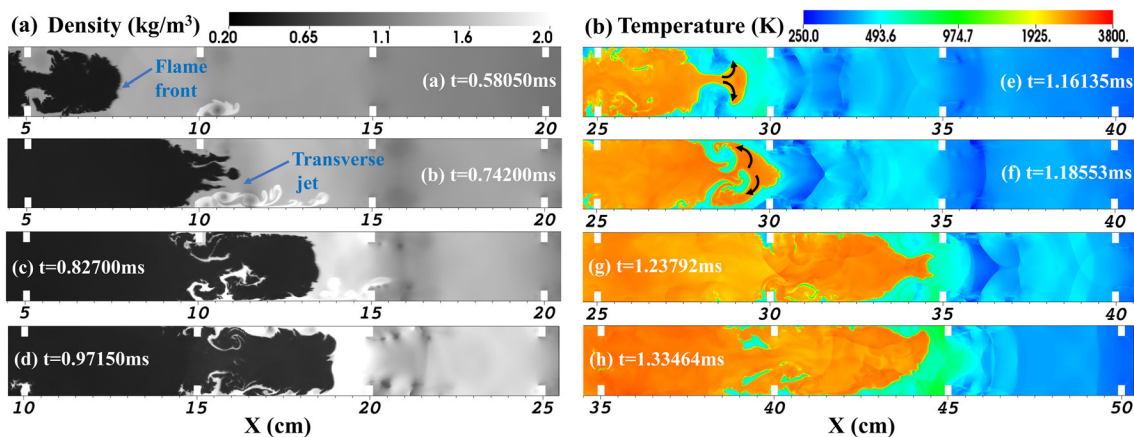


**FIG. 16.** Time evolution of the density contour and the subsequent temperature contour for case 5 [the left column is (a) density contour, while the right column is (b) temperature contour].

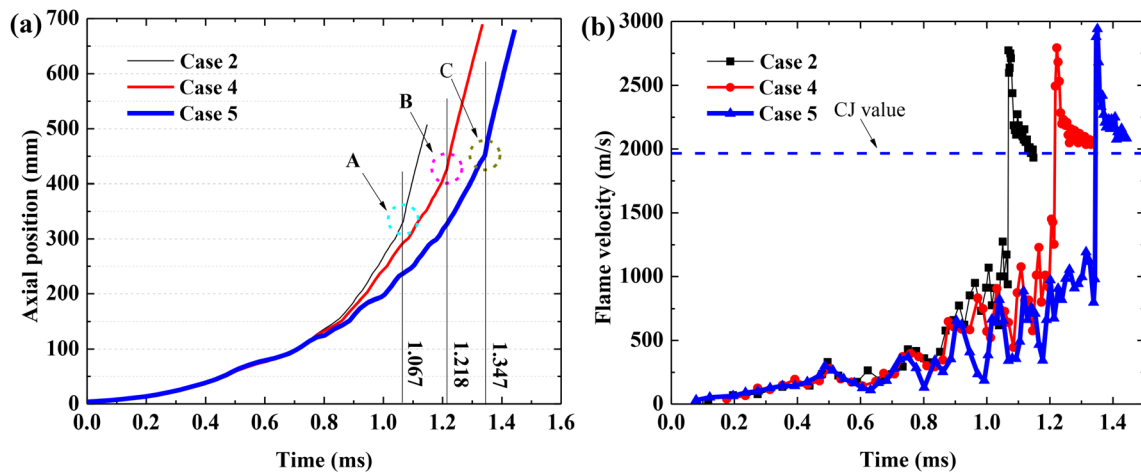


FIG. 17. (a) Axial position of the flame tip and (b) flame front velocity with time for different start time of the transverse jet after ignition (case 2:  $t = 0.001$ ; case 4:  $t = 0.25$ ; case 5:  $t = 0.5$  ms).

of turbulent flow and vortices to the single function of providing the required Br.

### E. The effect of jet stagnation pressure on flame acceleration and DDT

Figure 18 exhibits the variations of  $T_{DDT}$  and  $L_{DDT}$  with the increasing stagnation pressure of the transverse jet obstacle. When  $Br_j$  is increased from 2 to 3.5,  $T_{DDT}$  and  $L_{DDT}$  are reduced by 24.46% and 37.75%, respectively. However, when  $Br_j$  is raised to 5, it has a negative effect on the onset of detonation. Further increasing its pressure has a slight positive effect on the detonation transition, but the stagnation pressure of the jet has no significant effect on the  $T_{DDT}$  when its pressure increases from  $Br_j = 3.5$  to  $Br_j = 6.5$ . Therefore, just increasing the stagnation pressure does not have a positive influence on shortening  $L_{DDT}$  and  $T_{DDT}$  in the obstacle-laden combustion tube, and it even

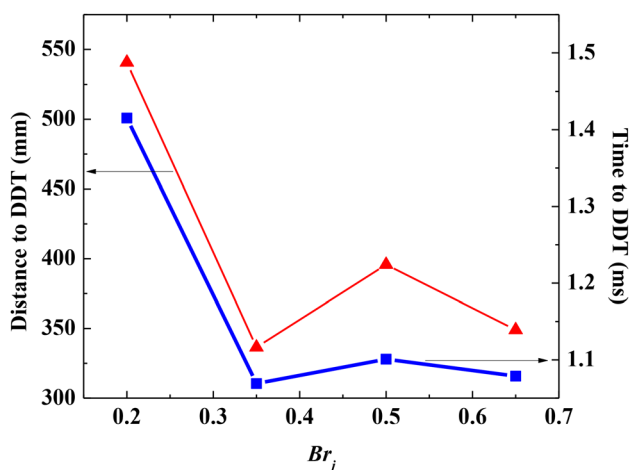


FIG. 18. The required DDT run-up time and DDT run-up distance as a function of the blockage ratio generated by the transverse jet.

has a negative effect. For further insight into these results, Fig. 19 presents the axial position of the flame front and the corresponding flame front propagation velocity as a function of time when varying the stagnation pressure. The flame tip in case 8 ( $P = 0.65$  MPa) is left behind compared to cases 2 and 6–8 before the onset of detonation, and this is also confirmed by the propagation velocity of the flame at the time range of  $t = 0.6$ – $0.8$  ms in circle J in Fig. 19(b). The flame acceleration rate in the next stage in case 8 is much higher as confirmed by Fig. 19(b). Next, the transition of detonation has occurred in cases 2, 8, and 7 consecutively as demonstrated by circles A–C in the zoomed figure; however, it needs more time to activate the DDT in case 6 as shown in circle D. The corresponding transition can also be observed in Fig. 19(b) as the curve of propagation velocity increases sharply, and then, the velocity decreases as the overdriven detonation is approaching the CJ detonation.

In general, as the stagnation pressure increases, the mass flow rate and flow momentum generated by the transverse jet increase, and the flow turbulence and vortices are enlarged accordingly. In other words, the extra energy generated by the flow perturbation region is enlarged. Such a feature can be confirmed by box A of the density contours for four cases at the same time of  $t = 0.68250$  ms in Fig. 20. As the jet stagnation pressure increases, the disturbance length in the chamber increases from 6.76 to 9.17 cm, as listed in Table IV. Yet, the increase rate of the disturbance area is not obvious when jet stagnation pressure is greater than 0.35 MPa. Those features have a positive effect on the flame acceleration when the flame tip approaches these turbulent regions thanks to the flame–turbulent interactions that increase the flame surface areas dramatically, as discussed in Sec. III A.

As shown in the pressure contours in the middle column of Fig. 20, with further augmentation of the jet pressure, the high-pressure regions are formed in the front of the flame tip (see series snapshots box B) and within the interval between obstacles. These results can be confirmed by the pressure distributions along the y-axial direction at  $Y = 9.5$  cm in Fig. 21(a), where much higher-pressure regions are formed in case 8, whereas the high-pressure regions are just located in the upper and lower tube in case 2. The static pressure within the tube



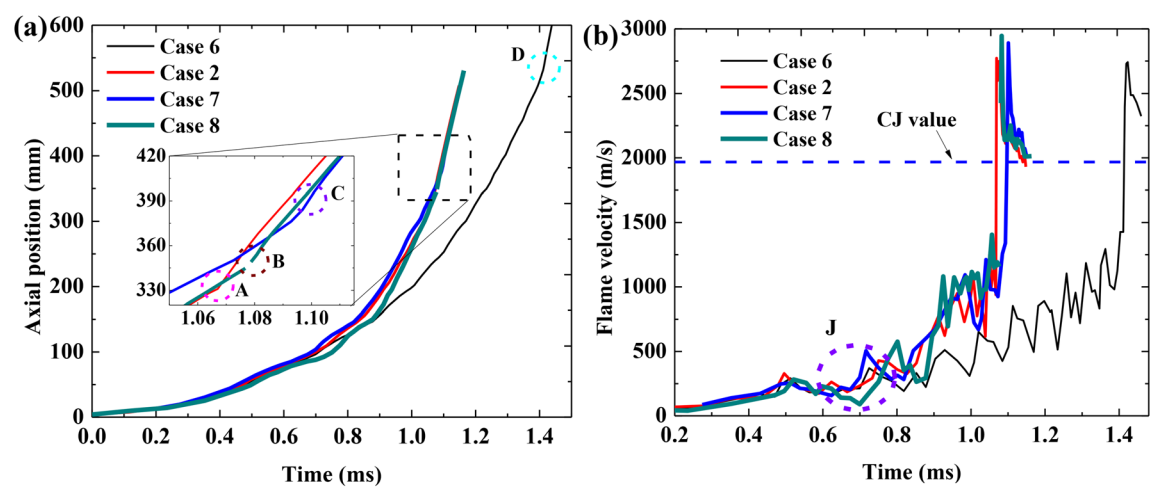


FIG. 19. (a) The axial position of the flame tip and (b) flame front propagating velocity with time evolution for different stagnation pressure of the transverse jet after mixture ignition (case 6:  $Br_j = 2$ ; case 2:  $Br_j = 3.5$ ; case 7:  $Br_j = 5$ ; case 7:  $Br_j = 6.5$ ).

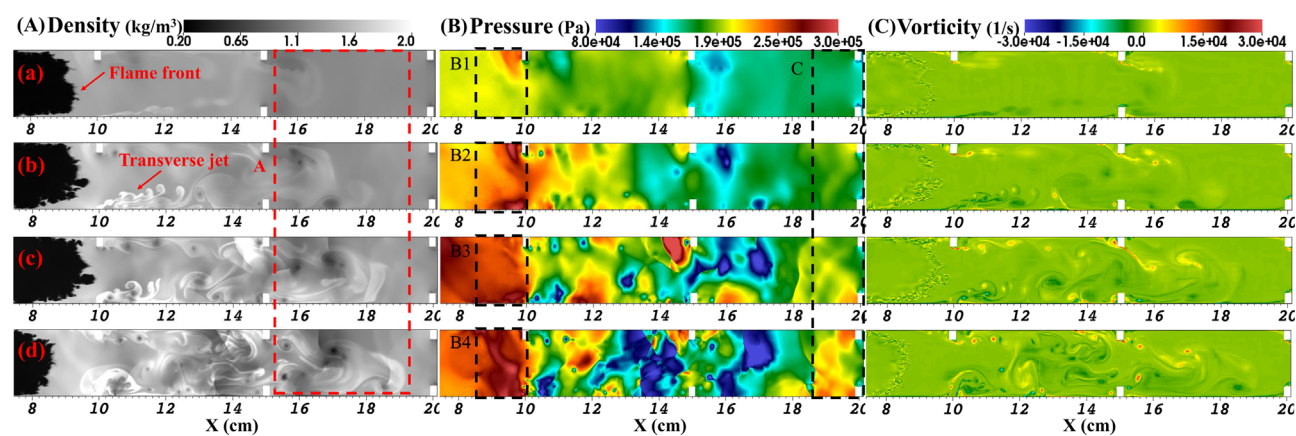


FIG. 20. Comparisons of density (A: left column), pressure (B: middle column), and vorticity (C: right column) contours at the same time of  $t = 0.68250$  ms for four cases with different jet stagnation pressure (the first row (a) is from case 6, the second row (b) is from case 2, the third row (c) is from case 7, and the lower row (d) is from case 8).

is also increased with the increase in the jet stagnation pressure, as listed in Table IV. These high-pressure regions located in the middle area of the tube restrain the flame acceleration when the flame tip approaches these areas, as confirmed by the snapshots of the flame

TABLE IV. The influence parameters generated by different jet stagnation pressure at  $t = 0.68250$  ms.

Case number	Stagnation pressure (MPa)	Disturbance length (cm)	Static pressure (MPa)	Maximum vorticity (1/s)
6	0.2	6.76	0.207 5	22 810
2	0.35	8.24	0.250 7	25 740
7	0.5	8.76	0.248 9	25 770
8	0.65	9.17	0.270 6	28 400

front in the density contours of Fig. 20 at the same time of  $t = 0.68250$  ms so that the flame propagation velocity is reduced sharply, especially in case 8 as confirmed by circle J in Fig. 19(b).

On the other hand, the intensity of compression wave and vorticity generated by the jet is increased with the augmentation of jet pressure in case 8 [see Figs. 22(b)–22(d)]. The vorticity variations along the central line are given in Fig. 21(b) for four cases at the same time of  $t = 0.68250$  ms, where a high vorticity amplitude is generated with the increase in jet pressure, and the maximum vorticity within the tube is also enhanced when increasing the jet pressure as listed in Table IV. These features have a positive effect on the flame acceleration when the flame front approaches the jet downstream; therefore, the flame acceleration rate increase in the next stage.

Furthermore, owing to the intense compression wave and high flame acceleration ratio, a strong leading shock wave is formed in the combustion tube. When the leading shock wave impacts a solid obstacle, the hot spot with high pressure and temperature in the corner of



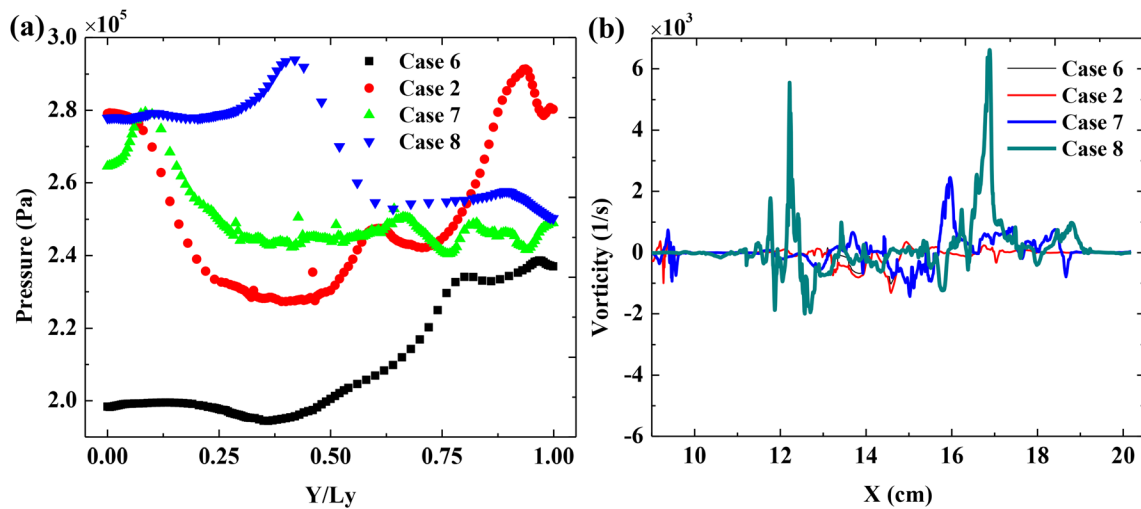


FIG. 21. Variations of the (a) pressure distributions along  $y$  direction at  $Y = 9.5$  cm and (b) vorticity along the central line of the tube for cases 6, 2, 7, and 8 at the same time of  $t = 0.68250$  ms.

the solid object is generated ahead of the flame tip; then, the onset of detonation is activated [see Fig. 22(g)]. This DDT can be explained as a classical hot spot-based initiation<sup>30,69</sup> through the gradient mechanism when the Mach stem is reflected from the solid wall. The evolution of DDT scenarios is demonstrated by the sequence of temperature contours in Figs. 22(g) and 22(h). Therefore, in terms of the case with high jet pressure, the flame acceleration generates a strong leading shock wave and Mach stem, which is sufficient to activate detonation after it reflects from a solid wall. The current DDT mechanism is consistent with the result obtained in Goodwin's study.<sup>53</sup>

In summary, the transverse jet introduces flow disturbance, vortices, local high static pressure, and compression waves. With the increase in the jet stagnation pressure, the flow disturbance and vortices are not the main reasons to affect the flame acceleration in the

obstacle-laden combustion tube. On the contrary, the local static pressure and compression wave have a more dominant effect on the flame acceleration, but the high local static pressure does not have a position influence on the flame acceleration before the flame front passes these high-pressure regions. Therefore, having a moderate stagnation pressure of the jet that generates appropriate flow disturbance, vortices, and compression waves in the obstacle-laden configuration is beneficial for shortening  $T_{DDT}$  and  $L_{DDT}$ .

#### IV. CONCLUSIONS

The unsteady reactive Navier–Stokes equations with a detailed chemistry reaction mechanism and an adaptive mesh refinement technique were employed to numerically simulate the flame acceleration and deflagration-to-detonation transition (DDT) processes in the current study. The turbulent flow and eddies were produced using a

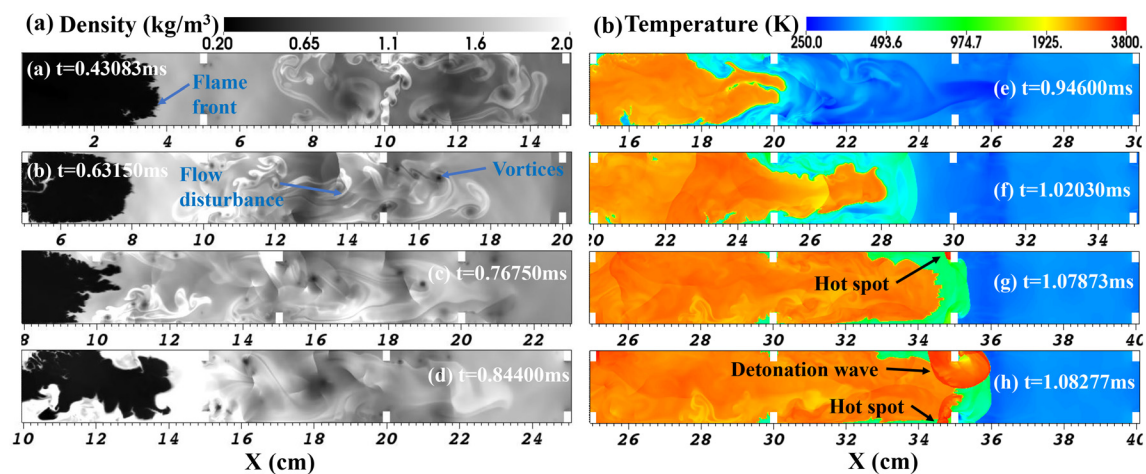


FIG. 22. The snapshots of the density contours and the subsequent temperature contours for case 8 [the left column is (a) density contour, and the right column is (b) temperature contour].

combination of transverse jet and solid obstacles. The effects of the start time of the transverse jet, the dual jet and solid obstacles, and jet stagnation pressure on the flame acceleration and DDT process were investigated to evaluate the efficiency of the flame acceleration. The main conclusions of the current study are as follows:

1. The combined fluid and solid obstacles arranged in a chamber significantly shorten the DDT run-up time and DDT run-up distance. The results for the combined case showed a 22.26% improvement in the DDT run-up time and a 33.36% reduction in the DDT run-up distance compared to that in the chamber with only solid obstructions. While just one width of domain size is considered in the current study, the scale effect should be further investigated, especially for large widths.
2. The mechanism of the flame acceleration in the combined obstacles is that the transverse jet stream can act as a solid obstruction that provides an appropriate blockage ratio. It also introduces large-scale turbulent flow and eddies in the downstream chamber. This further leads to more intense Kelvin–Helmholtz instabilities shedding from the tip of solid obstacles compared to the transverse jet injected into the smooth chamber in previous studies. The highly turbulent flame interactions and a subsequently stretched flame front are presented, resulting in a sharp augmentation of the propagation velocity with no conspicuous decrease when the flame front propagates to the unconfined space.
3. The dual jets injected into the chamber produce a lot of mushroom vortices and turbulent flow, which interact with the flame front and the fixed solid obstacle, resulting in a significantly stretched flame front and a lot of Kelvin–Helmholtz instabilities stemming from the solid tips. These outcomes result in a high flame propagation velocity and a shortened DDT run-up time.
4. A transverse jet with an early start time can act as a solid obstruction and in addition generates significant turbulent features and eddies downstream. With a more delayed start time, it only plays a role comparable to a solid obstruction.
5. A much higher jet stagnation pressure has a negative effect on shortening the run-up time to detonation in the obstacle-laden combustion tube. With the continuous increase of jet pressure, it is found that the DDT run-up distance cannot be further decreased, and it is even increased so that there is a moderate jet pressure value that results in the shortest DDT run-up time and DDT run-up distance.

Gamezo *et al.*<sup>14</sup> and Goodwin *et al.*<sup>53</sup> revealed that the flame acceleration and DDT mechanism in the two-dimensional (2D) and three-dimensional (3D) simulations are similar. The flame acceleration is dominated by the shock wave reflection. There is some difference in the leading shock wave that always decouples with the flame front. Moreover, the current flame–turbulent interaction occurs in the initial stage of flame acceleration so that there is still no formation of the shock wave. Hence, the jet obstacle has no significant effect in the next stage of flame acceleration. The jet diffusion and jet blockage ratio between 2D and 3D are still different; hence, 3D simulations of the combination of the transverse jet and solid obstacles on the flame acceleration rate should be further investigated.

## ACKNOWLEDGMENTS

This work was supported by the National Natural Science Foundation of China (Grant Nos. 11925207 and 91741205) and the China Scholarship Council (Grant No. 202106110005).

## AUTHOR DECLARATIONS

### Conflict of Interest

The authors have no conflicts to disclose.

### Author Contributions

**Wandong Zhao:** Writing – original draft (equal); Writing – review & editing (equal). **Jianhan Liang:** Funding acquisition (equal); Supervision (equal); Writing – review & editing (equal). **Ralf Deiterding:** Methodology (equal); Software (equal); Validation (equal); Writing – review & editing (equal). **Xiaodong Cai:** Software (equal); Writing – review & editing (equal). **Xinxin Wang:** Validation (equal); Visualization (equal).

## DATA AVAILABILITY

The data that support the findings of this study are available from the corresponding author upon reasonable request.

## REFERENCES

- <sup>1</sup>W. H. Heiser and T. Pratt, “Thermodynamic cycle analysis of pulse detonation engines,” *J. Propul. Power* **18**, 68 (2002).
- <sup>2</sup>G. D. Roy, S. M. Frolov, A. A. Borisov, and D. W. Netzer, “Pulse detonation propulsion: Challenges, current status, and future perspective,” *Prog. Energy Combust. Sci.* **30**, 545 (2004).
- <sup>3</sup>J. Shepherd and E. Wintenberger, “Thermodynamic analysis of combustion processes for propulsion systems,” AIAA Paper No. 2004-1033, 2004.
- <sup>4</sup>S. M. Frolov, V. S. Aksenov, V. S. Ivanov, I. O. Shamshin, and A. E. Zangiev, “Air-breathing pulsed detonation thrust module: Numerical simulations and firing tests,” *Aerosp. Sci. Technol.* **89**, 275 (2019).
- <sup>5</sup>M. V. Papalexandris, “Numerical simulation of detonations in mixtures of gases and solid particles,” *J. Fluid Mech.* **507**, 95 (2004).
- <sup>6</sup>G. Ciccarelli and S. Dorofeev, “Flame acceleration and transition to detonation in ducts,” *Prog. Energy Combust. Sci.* **34**, 499 (2008).
- <sup>7</sup>X. Cai, R. Deiterding, J. Liang, and Y. Mahmoudi Larimi, “Mechanism of detonation stabilization in supersonic model combustor,” *J. Fluid Mech.* **910**, A40 (2021).
- <sup>8</sup>C. M. Romick, T. D. Aslam, and J. M. Powers, “Verified and validated calculation of unsteady dynamics of viscous hydrogen–air detonations,” *J. Fluid Mech.* **769**, 154 (2015).
- <sup>9</sup>B. Zhang, N. Mehrjoo, H. D. Ng, J. H. Lee, and C. Bai, “On the dynamic detonation parameters in acetylene–oxygen mixtures with varying amount of argon dilution,” *Combust. Flame* **161**, 1390 (2014).
- <sup>10</sup>B. Zhang, V. Kamenskihs, H. D. Ng, and J. H. S. Lee, “Direct blast initiation of spherical gaseous detonations in highly argon diluted mixtures,” *Proc. Combust. Inst.* **33**, 2265 (2011).
- <sup>11</sup>S. B. Dorofeev, A. V. Bezmelnitsin, V. P. Sidorov, J. G. Yankin, and I. D. Matsukov, “Turbulent jet initiation of detonation in hydrogen–air mixtures,” *Shock Waves* **6**, 73 (1996).
- <sup>12</sup>C. Bai, B. Zhang, G. Xiu, Q. Liu, and M. Chen, “Deflagration to detonation transition and detonation structure in diethyl ether mist/aluminum dust/air mixtures,” *Fuel* **107**, 400 (2013).
- <sup>13</sup>Z. Wang, J. Lu, J. Huang, C. Peng, and L. Zheng, “Experimental investigation on the operating characteristics in a multi-tube two-phase valveless air-breathing pulse detonation engine,” *Appl. Therm. Eng.* **73**, 23 (2014).
- <sup>14</sup>V. N. Gamezo, T. Ogawa, and E. S. Oran, “Numerical simulations of flame propagation and DDT in obstructed channels filled with hydrogen–air mixture,” *Proc. Combust. Inst.* **31**, 2463 (2007).

- <sup>15</sup>J. D. Regele, D. R. Kassoy, M. Aslani, and O. V. Vasilyev, "Evolution of detonation formation initiated by a spatially distributed, transient energy source," *J. Fluid Mech.* **802**, 305 (2016).
- <sup>16</sup>H. Peng, Y. Huang, R. Deiterding, Z. Luan, F. Xing, and Y. You, "Effects of jet in crossflow on flame acceleration and deflagration to detonation transition in methane-oxygen mixture," *Combust. Flame* **198**, 69 (2018).
- <sup>17</sup>B. W. Knox, D. J. Forliti, C. A. Stevens, J. L. Hoke, and F. R. Schauer, "Unsteady flame speed control and deflagration-to-detonation transition enhancement using fluidic obstacles," AIAA Paper No. 2010-151, 2010.
- <sup>18</sup>Z. Wang, Y. Zhang, J. Huang, Z. Liang, L. Zheng, and J. Lu, "Ignition method effect on detonation initiation characteristics in a pulse detonation engine," *Appl. Therm. Eng.* **93**, 1 (2016).
- <sup>19</sup>C. N. Markides and E. Mastorakos, "Experimental investigation of the effects of turbulence and mixing on autoignition chemistry," *Flow, Turbul. Combust.* **86**, 585 (2011).
- <sup>20</sup>R. Starke and P. Roth, "An experimental investigation of flame behavior during explosions in cylindrical enclosures with obstacles," *Combust. Flame* **75**, 111 (1989).
- <sup>21</sup>M. Fairweather, G. Hargrave, S. Ibrahim, and D. Walker, "Studies of premixed flame propagation in explosion tubes," *Combust. Flame* **116**, 504 (1999).
- <sup>22</sup>R. Lindstedt and V. Sakthitharan, "Time resolved velocity and turbulence measurements in turbulent gaseous explosions," *Combust. Flame* **114**, 469 (1998).
- <sup>23</sup>Y. Huang, H. Tang, J. Li, and C. Zhang, "Studies of DDT enhancement approaches for kerosene-fueled small-scale pulse detonation engines applications," *Shock Waves* **22**, 615 (2012).
- <sup>24</sup>T. Li, X. Wang, B. Xu, and F. Kong, "An efficient approach to achieve flame acceleration and transition to detonation," *Phys. Fluids* **33**, 056103 (2021).
- <sup>25</sup>E. S. Oran and V. N. Gamezo, "Origins of the deflagration-to-detonation transition in gas-phase combustion," *Combustion and flame* **148**, 4 (2007).
- <sup>26</sup>A. Teodorczyk, P. Drobniak, and A. Dabkowski, "Fast turbulent deflagration and DDT of hydrogen-air mixtures in small obstructed channel," *Int. J. Hydrogen Energy* **34**, 5887 (2009).
- <sup>27</sup>A. Heidari and J. Wen, "Flame acceleration and transition from deflagration to detonation in hydrogen explosions," *Int. J. Hydrogen Energy* **39**, 6184 (2014).
- <sup>28</sup>M. Cross and G. Ciccarelli, "DDT and detonation propagation limits in an obstacle filled tube," *J. Loss Prev. Process Ind.* **36**, 380 (2015).
- <sup>29</sup>B. Zhang, H. Liu, and C. Wang, "Detonation velocity behavior and scaling analysis for ethylene-nitrous oxide mixture," *Appl. Therm. Eng.* **127**, 671 (2017).
- <sup>30</sup>E. S. Oran, G. Chamberlain, and A. Pekalski, "Mechanisms and occurrence of detonations in vapor cloud explosions," *Prog. Energy Combust. Sci.* **77**, 100804 (2020).
- <sup>31</sup>J. H. Lee, *The Detonation Phenomenon* (Cambridge University Press, 2008).
- <sup>32</sup>V. N. Gamezo, T. Ogawa, and E. S. Oran, "Flame acceleration and DDT in channels with obstacles: Effect of obstacle spacing," *Combust. Flame* **155**, 302 (2008).
- <sup>33</sup>V. N. Gamezo, C. L. Bachman, and E. S. Oran, "Flame acceleration and DDT in large-scale obstructed channels filled with methane-air mixtures," *Proc. Combust. Inst.* **38**(3), 3521–358 (2021).
- <sup>34</sup>Y. B. Zel'Dovich, V. B. Librovich, G. M. Makhviladze, and G. I. Sivashinsky, "On the development of detonation in a non-uniformly preheated gas," *Astronaut. Acta* **15**, 313 (1970).
- <sup>35</sup>J. Lee, R. Knystautas, and N. Yoshikawa, *Photochemical Initiation of Gaseous Detonations* (Elsevier, 1980).
- <sup>36</sup>R. Hall, A. Masri, P. Yaroshchik, and S. Ibrahim, "Effects of position and frequency of obstacles on turbulent premixed propagating flames," *Combust. Flame* **156**, 439 (2009).
- <sup>37</sup>D. Paxson, F. Schauer, and D. Hopper, "Performance impact of deflagration to detonation transition enhancing obstacles," AIAA Paper No. 2009-502, 2009.
- <sup>38</sup>M. Cooper, S. Jackson, J. Austin, E. Wintenberger, and J. Shepherd, "Direct experimental impulse measurements for detonations and deflagrations," *J. Propul. Power* **18**, 1033 (2002).
- <sup>39</sup>K. A. Ahmed and D. J. Forliti, "Fluidic flame stabilization in a planar combustor using a transverse slot jet," *AIAA J.* **47**, 2770 (2009).
- <sup>40</sup>D. A. Kessler, V. N. Gamezo, and E. S. Oran, "Simulations of flame acceleration and deflagration-to-detonation transitions in methane-air systems," *Combust. Flame* **157**, 2063 (2010).
- <sup>41</sup>B. Knox, D. Forliti, C. Stevens, J. Hoke, and F. Schauer, "A comparison of fluidic and physical obstacles for deflagration-to-detonation transition," AIAA Paper No. 2011-587, 2011.
- <sup>42</sup>S. Zhao, Y. Fan, H. Lv, and B. Jia, "Effects of a jet turbulator upon flame acceleration in a detonation tube," *Appl. Therm. Eng.* **115**, 33 (2017).
- <sup>43</sup>J. P. McGarry and K. A. Ahmed, "Flame-turbulence interaction of laminar premixed deflagrated flames," *Combust. Flame* **176**, 439 (2017).
- <sup>44</sup>J. Chambers and K. Ahmed, "Turbulent flame augmentation using a fluidic jet for deflagration-to-detonation," *Fuel* **199**, 616 (2017).
- <sup>45</sup>D. J. Tarrant, J. M. Chambers, P. H. Joo, and K. Ahmed, "Influence of transverse slot jet on premixed flame acceleration," *J. Propul. Power* **36**, 59 (2020).
- <sup>46</sup>S. M. Frolov, V. A. Smetanyuk, V. S. Aksenov, and A. S. Koval', "Deflagration-to-detonation transition in crossed-flow fast jets of propellant components," *Dokl. Phys. Chem.* **476**, 153 (2017).
- <sup>47</sup>H. Peng, Y. Huang, R. Deiterding, Y. You, and Z. Luan, "Effects of transverse jet parameters on flame propagation and detonation transition in hydrogen-oxygen-argon mixture," *Combust. Sci. Technol.* **193**, 1516 (2021).
- <sup>48</sup>J. Cheng, B. Zhang, H. Liu, and F. Wang, "The precursor shock wave and flame propagation enhancement by CO<sub>2</sub> injection in a methane-oxygen mixture," *Fuel* **283**, 118917 (2021).
- <sup>49</sup>J. Cheng, B. Zhang, H. Liu, and F. Wang, "Experimental study on the effects of different fluidic jets on the acceleration of deflagration prior its transition to detonation," *Aerosp. Sci. Technol.* **106**, 106203 (2020).
- <sup>50</sup>W. Zhao, J. Liang, R. Deiterding, X. Cai, and X. Wang, "Effect of transverse jet position on flame propagation regime," *Phys. Fluids* **33**, 091704 (2021).
- <sup>51</sup>R. Deiterding, *Parallel Adaptive Simulation of Multi-Dimensional Detonation Structures* (Brandenburgische Technische Universität Cottbus, Cottbus, 2003).
- <sup>52</sup>S.-Y. Lee, C. Conrad, S. Pal, R. Santoro, S. Saretto, J. Watts, and R. Woodward, "Deflagration to detonation transition processes by turbulence-generating obstacles in pulse detonation engines," *J. Propul. Power* **20**, 1026 (2004).
- <sup>53</sup>G. B. Goodwin, R. W. Houim, and E. S. Oran, "Effect of decreasing blockage ratio on DDT in small channels with obstacles," *Combust. Flame* **173**, 16 (2016).
- <sup>54</sup>D. G. Goodwin, H. K. Moffat, and R. L. Speth, *Cantera: An Object-Oriented Software Toolkit for Chemical Kinetics, Thermodynamics, and Transport Processes* (Caltech, Pasadena, CA, 2009).
- <sup>55</sup>H. D. Ng, Y. Ju, and J. H. Lee, "Assessment of detonation hazards in high-pressure hydrogen storage from chemical sensitivity analysis," *Int. J. Hydrogen Energy* **32**, 93 (2007).
- <sup>56</sup>X. Cai, J. Liang, R. Deiterding, Y. Mahmoudi Larimi, and M.-B. Sun, "Experimental and numerical investigations on propagating modes of detonations: Detonation wave/boundary layer interaction," *Combust. Flame* **190**, 201 (2018).
- <sup>57</sup>X. Cai, R. Deiterding, J. Liang, M. Sun, and Y. Mahmoudi, "Diffusion and mixing effects in hot jet initiation and propagation of hydrogen detonations," *J. Fluid Mech.* **836**, 324 (2018).
- <sup>58</sup>R. B. Bird, W. E. Stewart, and E. N. Lightfoot, *Transport Phenomena* (John Wiley & Sons, 2006).
- <sup>59</sup>S. Mathur, P. Tondon, and S. Saxena, "Thermal conductivity of binary, ternary and quaternary mixtures of rare gases," *Mol. Phys.* **12**, 569 (1967).
- <sup>60</sup>J. L. Ziegler, R. Deiterding, J. E. Shepherd, and D. I. Pullin, "An adaptive high-order hybrid scheme for compressive, viscous flows with detailed chemistry," *J. Comput. Phys.* **230**, 7598 (2011).
- <sup>61</sup>Y. Wang, Z. Chen, and H. Chen, "Propagation of gaseous detonation in spatially inhomogeneous mixtures," *Phys. Fluids* **33**, 116105 (2021).
- <sup>62</sup>H. Wei, X. Zhang, H. Zeng, R. Deiterding, J. Pan, and L. Zhou, "Mechanism of end-gas autoignition induced by flame-pressure interactions in confined space," *Phys. Fluids* **31**, 076106 (2019).
- <sup>63</sup>W. Chen, J. Liang, X. Cai, and Y. Mahmoudi, "Three-dimensional simulations of detonation propagation in circular tubes: Effects of jet initiation and wall reflection," *Phys. Fluids* **32**, 046104 (2020).
- <sup>64</sup>Y. Zhou, X. Zhang, L. Zhong, R. Deiterding, L. Zhou, and H. Wei, "Effects of fluctuations in concentration on detonation propagation," *Phys. Fluids* **34**, 076101 (2022).

- <sup>65</sup>R. Deiterding, "A parallel adaptive method for simulating shock-induced combustion with detailed chemical kinetics in complex domains," *Comput. Struct.* **87**, 769 (2009).
- <sup>66</sup>C. K. Westbrook, "Chemical kinetics of hydrocarbon oxidation in gaseous detonations," *Combust. Flame* **46**, 191 (1982).
- <sup>67</sup>M. Burke, M. Chaos, Y. Ju, F. Dryer, and S. Klippenstein, "Comprehensive  $H_2/O_2$  kinetic model for high-pressure combustion," *Int. J. Chem. Kinet.* **44**, 444 (2012).
- <sup>68</sup>X. Cai, J. Liang, R. Deiterding, Y. Che, and Z. Lin, "Adaptive mesh refinement based simulations of three-dimensional detonation combustion in supersonic combustible mixtures with a detailed reaction model," *Int. J. Hydrogen Energy* **41**, 3222 (2016).
- <sup>69</sup>A. Y. Poludnenko, T. A. Gardiner, and E. S. Oran, "Spontaneous transition of turbulent flames to detonations in unconfined media," *Phys. Rev. Lett.* **107**, 054501 (2011).
- <sup>70</sup>I. S. Yakovenko, A. Kiverin, and M. Liberman, "Flame acceleration and deflagration-to-detonation transition in three-dimensional rectangular channel," in 24th International Colloquium on the Dynamics of Explosions and Reactive Systems, 2013.
- <sup>71</sup>H. Xiao and E. S. Oran, "Shock focusing and detonation initiation at a flame front," *Combust. Flame* **203**, 397 (2019).
- <sup>72</sup>A. D. Kiverin, D. R. Kassoy, M. F. Ivanov, and M. A. Liberman, "Mechanisms of ignition by transient energy deposition: Regimes of combustion wave propagation," *Phys. Rev. E* **87**, 033015 (2013).
- <sup>73</sup>S. Maeda, S. Minami, D. Okamoto, and T. Obara, "Visualization of deflagration-to-detonation transitions in a channel with repeated obstacles using a hydrogen-oxygen mixture," *Shock Waves* **26**, 573 (2016).
- <sup>74</sup>J. Li, W.-H. Lai, K. Chung, and F. Lu, "Experimental study on transmission of an overdriven detonation wave from propane/oxygen to propane/air," *Combust. Flame* **154**, 331 (2008).
- <sup>75</sup>H. Xiao and E. S. Oran, "Flame acceleration and deflagration-to-detonation transition in hydrogen-air mixture in a channel with an array of obstacles of different shapes," *Combust. Flame* **220**, 378 (2020).
- <sup>76</sup>J. Cheng, B. Zhang, H. Dick Ng, H. Liu, and F. Wang, "Effects of inert gas jet on the transition from deflagration to detonation in a stoichiometric methane-oxygen mixture," *Fuel* **285**, 119237 (2021).
- <sup>77</sup>O. Y. Al-Thehabey, "Modeling the amplitude growth of Richtmyer-Meshkov instability in shock-flame interactions," *Phys. Fluids* **32**, 104103 (2020).